AGU Advances

RESEARCH ARTICLE
10.1029/2020AV000260

Inferring the Evolution of a Large Earthquake From Its Acoustic Impacts on the Ionosphere

P. A. Inchin[1], J. B. Snively[1], Y. Kaneko[2,3], M. D. Zettergren[1], and A. Komjathy[4]

[1]Center for Space and Atmospheric Research and Physical Sciences Department, Embry-Riddle Aeronautical University, Daytona Beach, FL, USA, [2]Department of Geophysics, Kyoto University, Kyoto, Japan, [3]GNS Science, Lower Hutt, New Zealand, [4]Jet Propulsion Laboratory, California Institute of Technology, Pasadena, CA, USA

Key Points:

- Numerical simulations of acoustic waves and ionospheric plasma disturbances driven by the M7.8 Kaikoura earthquake are performed
- Comparisons of simulations with TEC observations strongly suggest that the Papatea fault was ruptured during the Kaikoura earthquake
- TEC observations can supplement seismological studies of large crustal earthquake evolutions beyond traditional datasets

Supporting Information:

Supporting Information may be found in the online version of this article.

Correspondence to:

P. A. Inchin,
inchinp@erau.edu

Citation:

Inchin, P. A., Snively, J. B., Kaneko, Y., Zettergren, M. D., & Komjathy, A. (2021). Inferring the evolution of a large earthquake from its acoustic impacts on the ionosphere. *AGU Advances*, *2*, e2020AV000260. https://doi.org/10.1029/2020AV000260

Received 3 AUG 2020
Accepted 12 MAR 2021

Abstract We investigate the possibility to constrain the evolution of the 2016 M7.8 Kaikoura earthquake evolution based on Global Positioning System signal-derived ionospheric total electron content (TEC) perturbations, that represent plasma responses to infrasonic acoustic waves (IAWs) generated by surface motion. This earthquake exhibited unusual complexity and some first-order aspects of its evolution remain unclear; for example, how and when the Papatea fault (PF) and the corresponding large surface deformation occurred. For various earthquake models, a seismic wave propagation code is used to simulate time-dependent surface deformations, which then excite IAWs in a 3D compressible nonlinear atmospheric model, coupled with a 2D nonlinear multispecies ionospheric plasma dynamic model. Our preferred finite-fault model reproduces the amplitudes, shapes, and time epochs of appearance of detected TEC perturbations well. Additionally, the incorporation of the PF, ruptured during the earthquake, results in the closest agreement between simulated and observed near-zenith vertical TEC perturbations, whereas its absence shows significant discrepancy. This supports the hypothesis that the PF was ruptured during the Kaikoura earthquake. Furthermore, the IAWs and resulting ionospheric plasma disturbances contain additional information on the PF rupture progression, including the timing of initiation and propagation direction, indicating new opportunities to further constrain the PF rupture with low elevation angle "slant" TEC data. The results confirm the ability for TEC measurements to constrain evolutions of large crustal earthquakes to provide new insight beyond traditional seismic and geodetic data sets.

Plain Language Summary Earthquakes launch low-frequency infrasonic acoustic waves (IAWs) into the Earth's atmosphere. As they reach the ionosphere (~80–1,000 km altitude), IAWs may cause plasma disturbances detectable in the total electron content (TEC), which are routinely measured via fluctuations in Global Positioning System (GPS) signals. However, robust interpretations of coseismic ionospheric disturbances (CIDs) in TEC remain challenging due to the complexity of the coupled dynamics between the Earth's interior, atmosphere and ionosphere. We analyze the evolution of the 2016 New Zealand earthquake by comparing simulated and detected TEC perturbations. Novel model simulations, accounting for full physics of seismic waves, IAWs, and CIDs, show that the incorporation of the Papatea fault (PF) rupture during the earthquake results in the closest agreement between simulated and observed TEC. This supports the hypothesis that the PF was ruptured during the Kaikoura earthquake, which could not be constrained from available seismometer data. Our results suggest that IAWs and resulting CIDs are both sensitive to earthquake rupture progression. We conclude that the evolution of large earthquakes can be further investigated based on GPS TEC measurements combined with numerical physics-based simulations.

1. Introduction

Natural and anthropogenic hazards can be accompanied by the excitation of infrasonic acoustic waves (<20 Hz; hereafter, IAWs) in the Earth's atmosphere (Astafyeva, 2019; Hines, 1960; Press & Harkrider, 1962). Particularly, seismically induced surface deformations are well-known sources of IAWs that are generated at solid–air interfaces (Blanc, 1985; Bolt, 1964). IAW propagation and characteristics are controlled by atmospheric conditions, winds, as well as their nonlinear evolutions, and can be investigated through the analyses of fluctuations they produce in densities, temperatures, and pressures of air and the ionospheric plasma, as discussed below (Bittner et al., 2010; Leonard & Barnes, 1965; Meng et al., 2019). The coupled

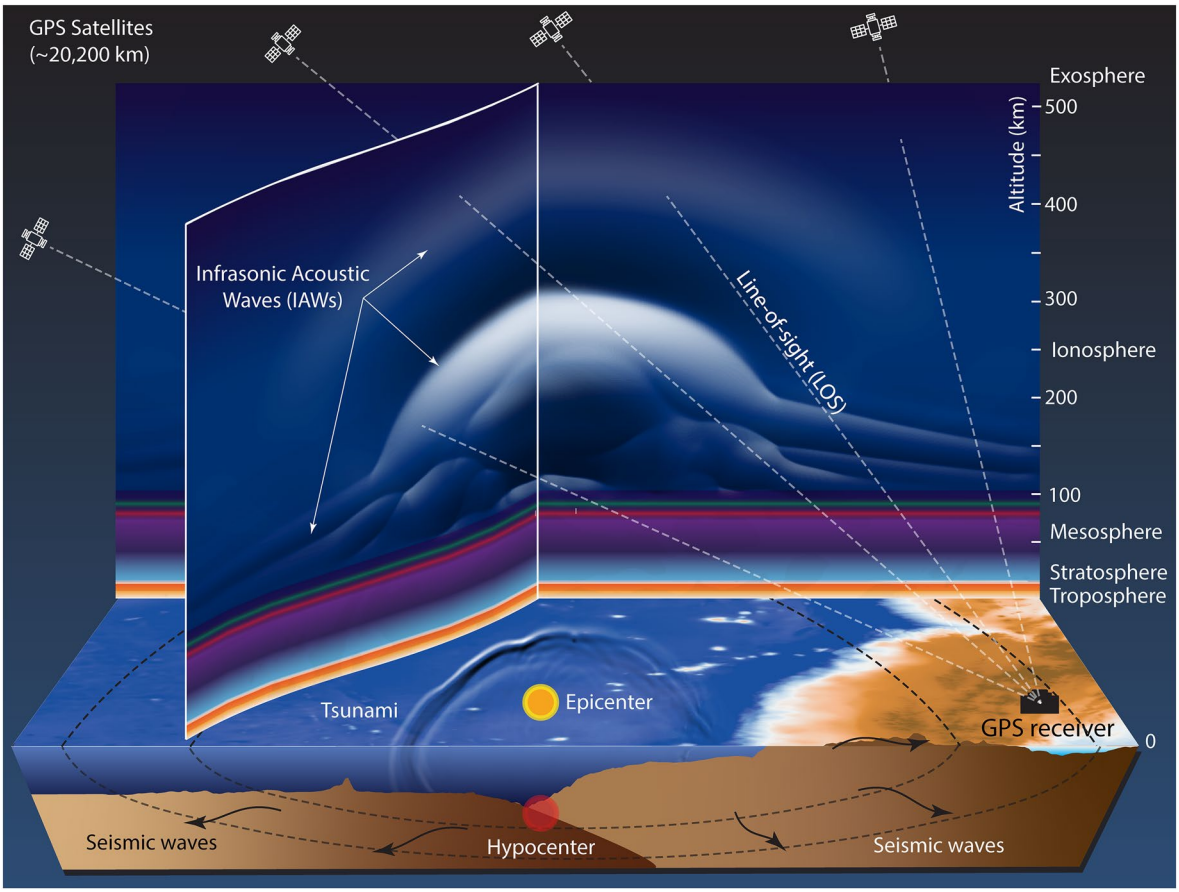

Figure 1. Schematic representation of earthquake–atmosphere–ionosphere-coupled geophysical processes. Seismically induced infrasonic acoustic waves (IAWs), excited at solid–air or water–air interfaces, propagate to the upper layers of atmosphere and generate ionospheric plasma disturbances. These disturbances can be detected with TEC observations that are based on the analyses of GPS signal degradation driven by ionospheric plasma. TEC represents the total number of electrons along line-of-sight (LOS) between GPS satellite and receiver. GPS, Global Positioning System.

nature of earthquake–atmosphere geophysical processes motivates important multidisciplinary studies and applications (Astafyeva & Shults, 2019; Occhipinti et al., 2013; Savastano et al., 2017).

Total electron content (TEC) observations remain one of the main sources of data used for indirect investigations of atmospheric waves in the upper atmosphere generated by natural hazards, such as earthquakes, tsunamis and volcano eruptions (Afraimovich et al., 2013; Azeem et al., 2017; Komjathy et al., 2016; Shults et al., 2016), and tornadoes and hurricanes (Chou et al., 2017; Nishioka et al., 2013). Representing the integrated number of free electrons between GPS satellite and the receiver along the line-of-sight (LOS) between them, TECs are based on measurements of group delays and phase advances of Global Positioning System (GPS) signals that propagate from GPS satellites to ground-based receivers through the dispersive ionized part of the upper atmosphere at ~80–1,000 km—ionospheric plasma (Parkinson et al., 1995). Reaching the upper atmosphere, atmospheric waves generate fluctuations in the ionosphere due to the interaction of air particles with plasma, and these fluctuations can be detected based on analyses of GPS signals (Figure 1). Growing networks of ground-based GPS receivers with high-rate data samplings (up to 50 Hz) provide hundreds to thousands LOSs with GPS satellites in their fields of view that are spatially and temporally sufficient for the investigation of small-scale and short-period IAW signals in the ionospheric plasma (e.g., Teunissen & Montenbruck, 2017).

Today, seismically induced IAWs, producing fluctuations in the ionospheric plasma, are routinely detected in TEC after large in-land and undersea earthquakes (Calais & Minster, 1998; Galvan et al., 2012; Y. Liu & Jin, 2019). However, TEC uncovers only a small part of coseismic IAW dynamics at far distances from their sources and their interpretations remain challenging (at ~250–350 km altitudes). Due to the complexity and

variety of dynamics that should be taken into account, from Earth's interior to the upper atmosphere and ionosphere, the majority of modeling studies are based on simplified approaches, for example, considering dynamics only in the atmosphere or ionosphere, with analytical solutions for linear IAW propagation from the ground (Matsumura et al., 2011; Rolland et al., 2011). In addition, the common approach of the use of point or axisymmetric (evenly distributed) IAW source models precludes the investigation of a broad range of phenomena, for example the propagation of rupture—slips in the Earth's crust during the earthquake (Meng et al., 2018; Thomas et al., 2018; M. D. Zettergren et al., 2017). Thus, comprehensive modeling studies that quantify the dynamics of IAWs and induced coseismic ionospheric plasma disturbances (CIDs) are a necessary step toward deeper understanding of coupled geophysical processes.

Here, we present new analyses of IAW dynamics and corresponding CIDs generated by the 2016 M7.8 Kaikoura earthquake in New Zealand. The earthquake exhibited unusual complexity, with some first-order aspects of its evolution remaining unclear to date, despite the availability of a wide range of geophysical data sets (e.g., Hamling et al., 2017). We address some of the limitations by investigating the ability of different finite-fault models, that represent the earthquake's spatial and temporal progression, to reproduce the observed TEC perturbations. Our approach combines three state-of-the-art full-physics-based numerical simulation techniques to model (1) seismic wave propagation and surface deformation, (2) excitation and propagation of IAWs in the atmosphere from ground to 500 km altitude, by where they are dissipated, and (3) ionospheric plasma responses to IAWs. We then compare simulation results with observed TEC perturbations and examine the validity of modeling approach and the sensitivity of the resulting TEC signatures to the parameters of finite-fault models.

The paper is divided into following sections. Section 2 provides an overview of the Kaikoura earthquake and detected CIDs with TEC observations. Modeling approach, assumptions, and parameters are described in Section 3. Section 4 contains the analyses of IAW dynamics and corresponding CIDs and the sensitivity of TEC perturbations to various finite-fault models. Discussion of the results and uncertainty analyses are provided in Section 5, and a summary of the study and future opportunities in Section 6.

2. The 2016 M7.8 Kaikoura Earthquake

2.1. Earthquake Characteristics

The 2016 M7.8 Kaikoura earthquake occurred in the northern South Island of New Zealand, in the area known as the Marlborough fault system, characterized by the tectonic transition from the Hikurangi subduction zone in the northeast to the Alpine fault zone in the southwest (Van Dissen & Yeats, 1991; Wallace et al., 2012). The Global Centroid Moment Tensor solution provides the epicenter of 42.74°S/173.05°E, and the origin time (T_0) of 00:02:56 local time November 14, 2016 (11:02:56 UT November 13, 2016). This event is considered as one of the most complex in-land earthquakes ever recorded (Hamling et al., 2017). Up to ∼12–20 ruptured fault segments have been identified from observations, some of which were previously unknown or considered inactive (Hamling et al., 2017). The faulting area extends to ∼180 km from the southwest to the northeast with the vertical surface deformation of up to ∼10 m locally (Clark et al., 2017; Litchfield et al., 2018). The overall earthquake progression was fairly slow, as it took ∼90 s for the rupture to propagate from the hypocenter (the position within the Earth where rupture initiates), located near its southern end, to its northern end (Cesca et al., 2017; Holden et al., 2017).

Finite-fault models, developed in previous studies, suggest that the earthquake rupture initiated on the Humps fault, propagated through southern faults, including the Leaders, Hundalee, and offshore Point Kean faults, and then onto the northern faults, including the Jordan, Kekerengu, Papatea, and Needles faults (Figure 2d) (Ando & Kaneko, 2018; Bai et al., 2017; Cesca et al., 2017; Holden et al., 2017; Ulrich et al., 2019; Wang et al., 2018). The moment magnitude of this event is estimated to be 7.8–7.9. Vertical surface deformation, derived from Interferometric Synthetic-Aperture Radar (InSAR) data from the Sentinel-1A satellite, suggests three primary zones of large surface uplifts: (1) around 2–3 m uplift in the vicinity of the Humps fault, (2) >5 m uplift in the south of the Papatea fault, and (3) a broader uplift zone in the north and northwest of the Papatea, Jordan, Kekerengu, and Needles faults (Figure 2c).

Due to the unusual complexity, previously published earthquake finite-fault models show significant disagreement in the details of how the rupture propagated. In particular, they show that the observed

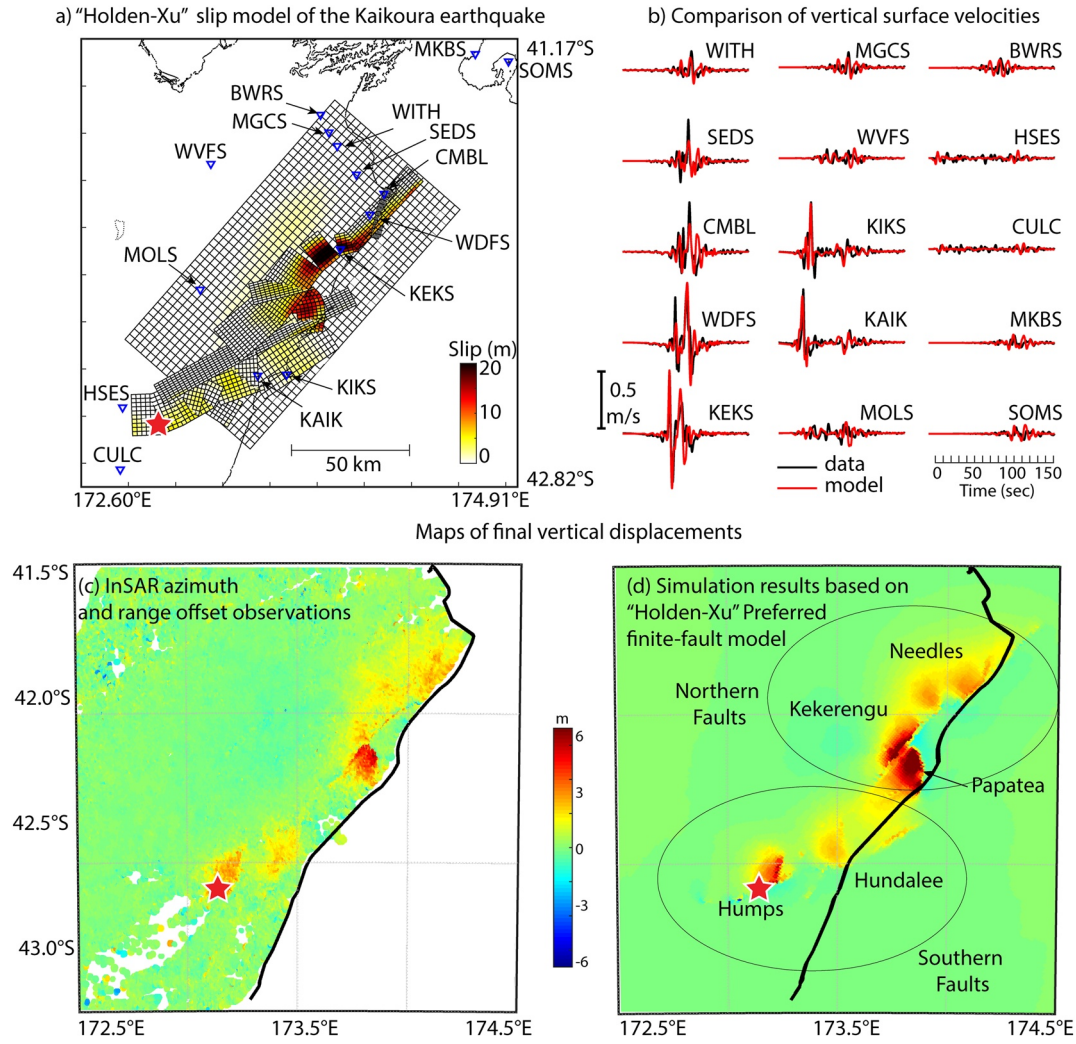

Figure 2. (a) "Holden–Xu" slip model of the Kaikoura earthquake with the indication of names and locations of near-epicentral cites. (b) Comparison of observed and synthetic vertical velocity seismograms, band pass filtered between 3 and 100 s, for selected near-epicentral strong motion and GPS cites. Vertical surface displacement field obtained from (c) Interferometric Synthetic-Aperture Radar (InSAR) observations and (d) seismic wave propagation simulation based on "Holden–Xu" preferred finite-fault model with the indication of main ruptured faults and areas. The color scale on plots (c) and (d) is oversaturated for better visibility of small features. The red star is positioned at the epicenter. GPS, Global Positioning System.

seismograms can be reproduced without including the Papatea fault (Holden et al., 2017), while other studies indicate that the Papatea fault ruptured during the Kaikoura earthquake, starting at ~30 s after T_0 (Wang et al., 2018), or simultaneously with Kekerengu fault at ~60 s after T_0 (Archuleta et al., 2018). The difficulty in identifying and isolating seismic signals generated by the Papatea fault is also hinted from the absence of its imprints in local seismic and high-rate GPS data around the Papatea fault (Tan et al., 2019; Zhang et al., 2017) and in backprojections (type of processing that images the source of seismic waves coherently recorded at stations throughout the seismic network, e.g., Kiser & Ishii, 2017). While some studies argue that elastic dislocation (slip) models fail to explain the observed surface deformation pattern (Diederichs et al., 2019; Tan et al., 2019; Zhang et al., 2017), others attempt to match the deformation data as best as feasible (Xu et al., 2018). Note that the earliest satellite InSAR image data were acquired a few days after the earthquake (Hamling et al., 2017), which constrains the timing of Papatea fault rupturing to be within the first few days. Yet, it remains unclear *when (coseismic or early postseismic aftershock) and how (seismically or aseismically) the Papatea fault was ruptured*. A better understanding of the rupture evolution of this complex event is important for seismology and future earthquake and tsunami hazard assessment globally.

2.2. Observable TEC Perturbations

Several studies reported the characteristics of TEC perturbations generated by coseismic IAWs during the Kaikoura earthquake (Bagiya et al., 2018; Lee et al., 2018; Li et al., 2018). We reanalyze observed CIDs, particularly for the purposes of model result validation and to test hypotheses on the Papatea fault evolution. We use 1 Hz data from 72 ground-based receivers on the territory of New Zealand operated by New Zealand's GeoNet. Slant TEC (TEC along the LOS between GPS satellite and receiver; hereafter sTEC) and vertical TEC (the projection of sTEC onto the LOS between the center of the Earth and GPS satellite position, which is used to normalize sTEC observations from different GPS satellite-receiver pairs; hereafter vTEC) are calculated using Jet Propulsion Laboratory software from raw data in Receiver Independent Exchange Format (RINEX) (Komjathy et al., 2005). We refer to TEC observations belonging to satellite-receiver pairs by indicating pseudo-random noise (PRN) sequence number, assigned to each GPS satellite, and receiver name, for example PRN20-AVLN. For the calculation of ionospheric pierce point (IPP) coordinates, that represent the positions where LOS between GPS satellite and receiver traverses the altitude of electron density peak in the ionosphere and are used for the georeferencing of TEC observations, we choose height at 300 km. Here, we discuss TEC observations from receivers with four GPS satellites: PRN20 and 29 with elevation angles of LOS of 70°–85° with chosen receivers, PRN21 with LOS elevation angles of 30°–50°, and PRN05 with LOS elevation angles of 25°–50° and IPPs offshore to the east from South Island of New Zealand. Available observables with GPS PRN13 and GLONASS satellites do not provide additional insight for our investigation but were addressed in studies referenced above.

Demonstrative vTEC time series are combined in Figure 3. vTEC perturbations, shown in vertical panels a and b, are derived by applying a 10-s to 10-min band-pass Butterworth filter. They are supplemented by wavelet transform evolutions underneath time series for 0–600 s range of periods. Plots are sorted to show observations to the west from the epicenter on panel a and to the east on panel b, with observations to the north at the top and observations to the south at the bottom. Panels c–f show vTEC time series for four satellite-receiver pairs to provide an overview of values and gradients above New Zealand during and after the earthquake. All plots are limited by 11:00–12:00 UT time range. On panel g, we depict tracks of IPP coordinates for the same time interval with colors related to the amplitudes of vTEC perturbations to represent the positions of CID detection. Our and previous studies demonstrate that the near-epicentral region was sufficiently covered by TEC observations for the detailed analysis of earthquake–ionosphere-coupled processes, what makes this event to be of high interest for investigation.

During the earthquake, vTEC at the region of New Zealand was fairly small due to local nighttime, ~7.0–12 TECu (1 TECu = 10^{16} el m^{-2}), with positive gradients from the south to the north (Figures 3e and 3f). Zonally, vTEC decreased from the west to the east, following the nighttime trend (Figures 3a and 3b). Based on observations, we estimate vTEC as 8.5–9.7 TECu in the region around epicentral area (e.g., PRN20-AVLN/LEVN) and ~10–11 TECu to the northern part of North Island (PRN29-CKID).

Strong CIDs were detected to the north and northeast from the epicentral area (PRN20-AVLN/KORO/MTQN, as well as in Figure 7e) and reached ~0.45 TECu peak-to-peak (ptp) or ~2%–3% from the background. TEC perturbations to the northeast and near to northern faults exhibited a practically pure N-wave shape (PRN20-MTQN/KORO), as expected shapes of CIDs generated by acoustic shock N-waves (hereafter N-waves), since their pressure profiles closely resemble "N," and they evolve due to nonlinear effects on IAWs (e.g., Whitham, 1974). Farther from the epicentral area to the northeast, as shown for pair PRN20-CKID, CIDs are still comparatively strong, but their N-wave shape is distorted. Moving to the west, vTEC perturbations are weaker—~0.2–0.23 TECu ptp (PRN20-OKOH/WITH/CMBL/TKHL, PRN29-TRWH/MAHA). Perturbations, detected farther to the west and southwest from the epicentral area, possess stronger initial depletion phases than enhancements (e.g., PRN20-CMBL/TKHL/YALD). Perturbations of ~0.03–0.1 TECu were detected offshore to the east (PRN05-KAIK/TKHL) and were proposed to be also driven by coseismic IAWs (Bagiya et al., 2018).

In summary, analyzing the available TEC observations, we find that there is a general trend of the strongest CIDs to the north and northeast with weak CIDs to the northwest. TEC perturbations exhibit periods of ~4–7 min and appear ~10 min after the earthquake, which is consistent with a time of IAW arrivals to the altitude of 250–300 km from the ground. As expected, the weakest CIDs were detected to the south from the

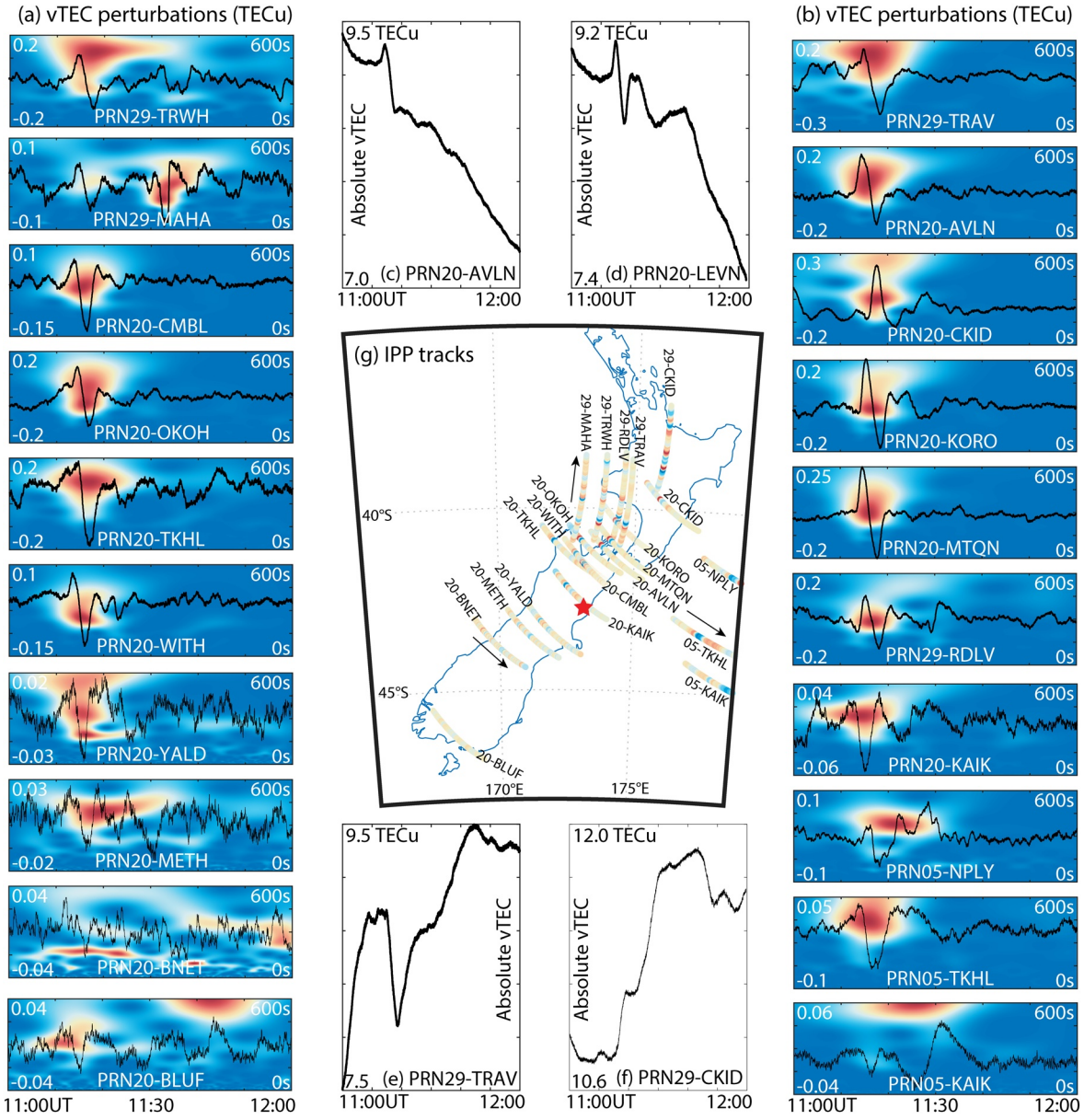

Figure 3. (a, b) vTEC observations filtered with 10-s to 10-min band-pass Butterworth filter and their wavelet transform evolutions for 0–10 min range of periods. (c–f) vTEC time series for GPS PRN20 with receivers AVLN and LEVN and GPS PRN29 with receivers TRAV and CKID. (g) IPP tracks for vTEC observations shown in panels (a)–(f). Arrows represent IPP motion directions. vTEC, vertical total electron content; GPS Global Positioning System; IPP, ionospheric pierce point.

epicentral area poleward, due to the dominant mobility of ionospheric plasma along magnetic field lines (e.g., M. D. Zettergren & Snively, 2015), precluding notable plasma drift driven by IAWs to the south (in a configuration of magnetic field lines over New Zealand).

3. Modeling Approach and Assumptions

For the reconstruction of near-epicentral surface deformation (and corresponding IAWs in the atmosphere), it is important to consider finite-fault models (Igel, 2017; Lay & Wallace, 1995). We test seven finite-fault models and find that one in particular best-reproduces observed surface deformation and TEC perturbations, to an extent that is significant. Throughout this manuscript, we will refer to this model as the "Holden–Xu" preferred model. It combines the finite-fault model of Holden et al. (2017) (Model A shown in their

study) and the Papatea fault model shown by Xu et al. (2018) with the specification of rupture propagation on the Papatea fault as discussed in this section. We first describe the results of simulations based on the "Holden–Xu" preferred model and the results based on other models are discussed in Section 4.3.

The original Holden finite-fault model was derived from seismic wave propagation simulations using the spectral-element solver SPECFEM3D Cartesian (Komatitsch & Tromp, 2002; Komatitsch & Vilotte, 1998) with 3D seismic wave velocity and attenuation models of New Zealand (Eberhart-Phillips et al., 2015, 2017), as well as regional topography and bathymetry (Becker et al., 2009). Additional details of seismic wave simulation method are provided in the Supporting Information. Initial finite-fault geometry and slip (displacement) distribution were based on results from Clark et al. (2017). Due to relatively minor contribution of the Papatea fault to local seismic observations (strong motion and GPS waveforms), the original model did not include this fault, despite the large surface deformation seen in the InSAR data (Figure 2c). In the Holden–Xu model, we take nonplanar fault geometry and slip distribution of the Papatea fault, presented in Xu et al. (2018), assume that the rupture on the Papatea fault nucleates (e.g., starts propagating) at T_0 + 57 s at its southern end and propagates to north with an average speed of 1.5 km/s, and add this Papatea fault model to the original Holden model. The slip distribution of the Holden–Xu model is shown in Figure 2a and the comparison of observed and simulated vertical surface velocities for selected near-epicentral stations is presented in Figure 2b. In this source model, the maximum slip on the Papatea fault is 16 m. The total moment magnitude of the simulated earthquake is Mw = 7.9. The small contribution of seismic moment (Mw = 7.3) and slow rupture speed lead to small seismic signals from the Papatea fault, relative to the large moment release on the Jordan–Kekerengu–Needles faults, and hence the simulated waveforms at near-epicentral stations are essentially the same as in those shown in the original Holden model. The Supporting Information provides comparison for other seismic stations, as well as the horizontal components of velocity waveforms. The map of final vertical surface deformation, resulting from the SPECFEM3D simulation with the Holden–Xu model, is shown in Figure 2d. Compared to the original Holden model, the Holden–Xu model better reproduces the InSAR-derived vertical deformation around the Papatea fault (see Figure SP2.pdf in the Supporting Information).

In the Holden–Xu preferred model, the rupture originates on the Humps fault at T_0 = 11:02:56 UT and propagates predominately toward the northeast at a rupture velocity of ~1.9 km/s on the Hundalee fault. The rupture then moves onto the offshore, Point Kean fault at T_0 + 31 s, and then continues onto the northern faults, including Upper Kowhai, Kekerengu, and Needles at a velocity of ~2.0 km/s. As in the original Holden model, the Holden–Xu model incorporates rupture reactivation at the southern segment of the Kekerengu fault with the rupture velocity of ~1.5 km/s, producing large surface deformation. This rupture reactivation, which was supported by other kinematic source inversion approach (Model B from Holden et al. [2017]), helps to explain two dominant seismic signals observed at near-epicentral stations (Figure 2b). While the Hikurangi subduction interface is included in the Holden–Xu model, there is little (~8%) contribution from slip on it to the overall moment. The total rupture process takes ~90 s, with the largest seismic moment release on the northern faults occurring at T_0 + (60–80) s.

We include offshore displacements to simulations without considering the propagation of hydro-acoustic waves in the ocean interior. For the shallow ocean region above the Point Kean fault (~<2 km), the water–air interface can be considered as transparent (Godin, 2006; McDonald & Calvo, 2007), resulting in practically the same ocean surface displacements as displacements at the ocean bottom (Levin & Nosov, 2016; Satake, 1987; T. Saito, 2019), taking into account that wavelength of resolved seismic waves is longer than ~20 km.

To simulate IAWs and ionospheric plasma disturbances, we follow an approach similar to that discussed in Inchin, Snively, Zettergren, et al. (2020). For this investigation, simulated surface vertical deformations are first obtained from a numerical forward seismic wave propagation simulation as described above, for the domain of 600 × 600 km around epicentral area from T_0 to 200 s. Then, surface deformations are regridded, reinterpolated, differentiated, and used to impose vertical velocity lower boundary conditions for the 3D compressible nonlinear atmospheric Model for Acoustic-Gravity wave Interactions and Coupling (MAGIC) (Snively, 2013). These are mapped over the horizontal domain 900 × 900 km in latitude and longitude, with an altitude span of 500 km, at resolution of 1 and 2 km in horizontal and 0.25 km in the vertical directions. After 200 s, we set a reflective boundary condition at the ground surface boundary to enable realistic IAW

reflections at later times. The profiles of meridional and zonal winds, temperature, and major species densities (O, O_2, N_2 that constitute >99% of atmospheric density) at T_0 are derived from empirical models HWM-14 and NRLMSISE00, respectively (Drob et al., 2015; Picone et al., 2002).

For the simulation of ionospheric responses to IAWs, we use the 2D nonlinear ionospheric plasma dynamic model GEMINI (M. Zettergren & Semeter, 2012), which solves a full set of conservation equations for the major ionospheric species ($s = O^+, NO^+, N_2^+, O_2^+, N^+, H^+$, and e). The perturbations of atmospheric densities, temperature, and fluid velocities, computed in MAGIC, are specified time dependently (via interpolation in space and time) as an input to GEMINI (M. D. Zettergren & Snively, 2015). An initial ionospheric plasma state, prior to the earthquake, is calculated based on the GEMINI simulation self-consistently. The schematic representation of numerical domains is shown in Figure 6h.

4. Simulation Results

4.1. IAW Dynamics

First, we examine the nature of the earthquake evolution and surface deformation by quantifying different fault contributions to resulting IAW wavefields. Figure 4 shows simulated IAWs for four earthquake finite-fault models: (1) the Holden–Xu preferred model, (2) Holden–Xu model without Papatea fault contribution, (3) the Holden–Xu model without northern faults contribution, and (4) isolated Papatea fault. This figure shows horizontal plane slices of vertical fluid (flow) velocities at two altitudes—75 km (left column) and 250 km (middle column), representing the upper mesosphere and bottom part of ionospheric F-layer, where TEC perturbations occur. The rupture propagation direction on the Papatea fault in all these cases is assumed to be from the south to the north, which is the same as in the preferred Holden–Xu model. Animations for each of the simulations are included in the Supporting Information.

Our modeling results suggest that two main areas of surface deformation, around the Humps fault in the southwest and around the Papatea and Kekerengu faults in the northeast (Figure 2c), contribute to IAWs in the atmosphere. Bagiya et al. (2018) and Lee et al. (2018) attributed these areas as the source of observed TEC perturbations. Our modeling results are consistent with their findings, in that comparatively weak and strong IAWs are excited around southern and northern faults, respectively (Figure 4a). Two radiations of strong IAWs, originating from the northern faults, can be discerned at 75 km altitude. The first one corresponds to IAWs of comparatively small amplitudes to the north-northeast by earlier ($T < 55$ s) surface deformation associated with the Kekerengu and Needles fault rupture. The second, strongest IAWs are excited by the later ($T > 55$ s) surface deformation associated with both the Papatea fault rupture and the rupture reactivation on the Kekerengu fault (Figures 4a and 4d). Vertical fluid velocities of IAWs peak at 277 m/s at 250 km altitude, such that nonlinearity—leading to acoustic shock formation—is important in their propagation. The simulation with only the southern faults show comparatively weak IAWs, though still contributing to IAWs to the north and northeast (Figures 4g–4i).

Vertical surface deformation around the Papatea fault drives IAWs in the atmosphere with vertical fluid velocities up to 130 m/s (Figures 4j–4l) at 250 km altitude that substantially contribute to the wavefield. At 75 km, the amplitudes of arrived IAWs to the northeast with and without Papatea fault contributions differ markedly (Figures 4a and 4d, respectively), and at 250 km the difference of vertical fluid velocities to the north-northeast is ~50 m/s (Figures 4b and 4e).

The spatial asymmetry of IAWs can be seen throughout the whole range of altitudes (Figures 4b, 4e and 4h). At ionospheric F-layer heights (>200 km), differentiating between IAWs from individual fault segments is complicated, due to the interference of nonlinear IAWs, the substantial increase of IAW wavelengths above ~120 km due to the increase of atmospheric temperature, and the thermo-viscous dissipation that markedly damps and smooth IAWs. Nevertheless, their overall dynamics can still be discerned. The first emergence of IAWs is directed to the northeast and is related to surface deformation around the southern faults (Figure 4c). Later on, there is an arrival of much stronger IAWs from the northern faults with a slight rotation of the wavefront of the strongest IAWs to the north-northeast (Figure 4b). The direction of rupture propagation plays a role in the IAW asymmetry even for very localized surface deformation at the Papatea fault (Figures 4j–4l). Figures 4f and 4l present snapshots at early arrival times of IAWs. Here, IAWs excited by the strong permanent surface deformation at the epicentral area, as well as by transient surface displacement

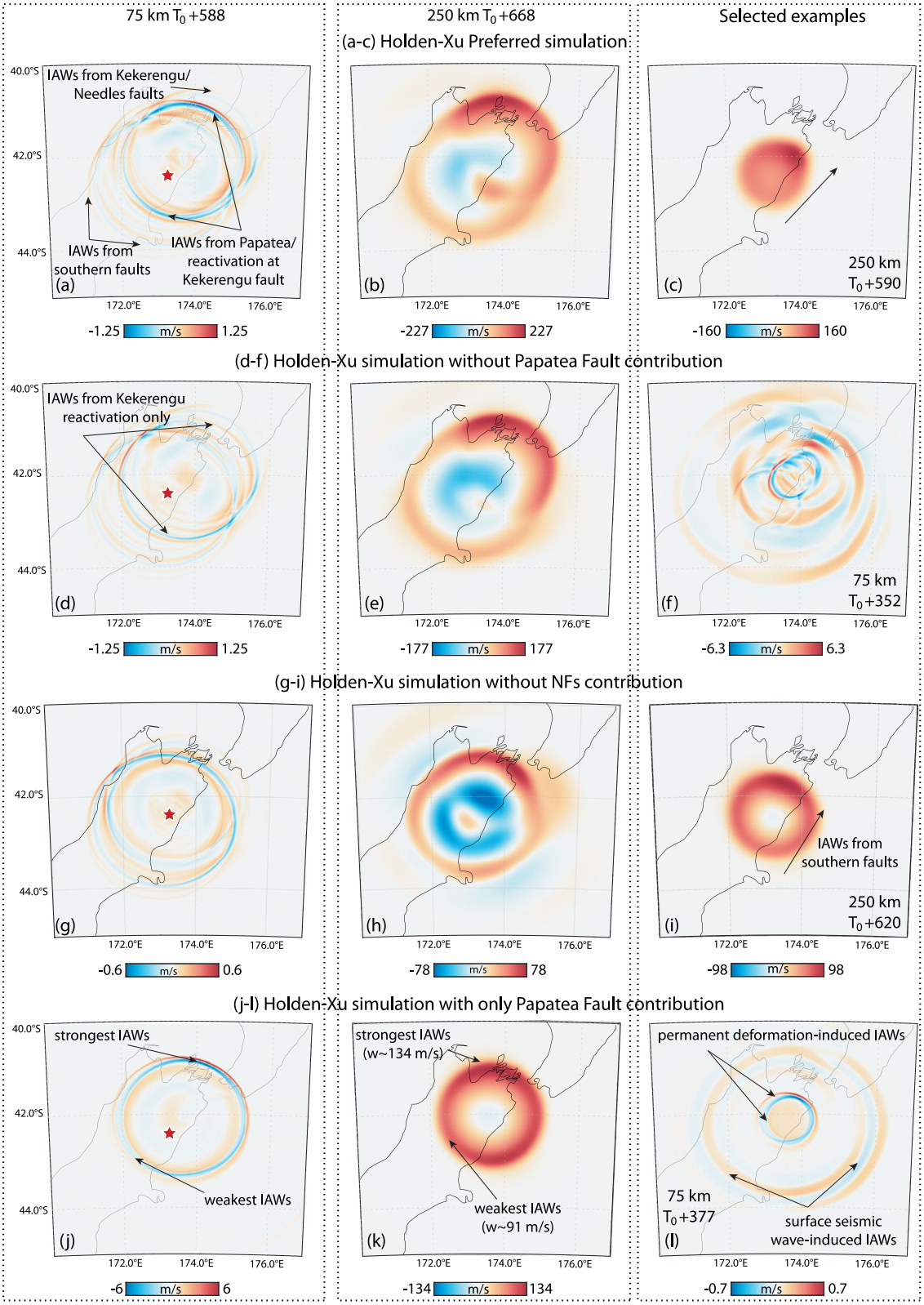

Figure 4. Simulated vertical atmospheric fluid (flow) velocities at 75 and 250 km altitudes for four different configurations of the Holden–Xu model: (a–c) the preferred model, (d–f) the model without the Papatea fault, (g–i) the model that includes the southern faults only, and (j–l) the model with an isolated Papatea fault. Left column includes snapshots at 75 km altitude at T_0 + 588 s and middle column—snapshots at 250 km altitude at T_0 + 668 s. The red star shows the epicenter of the earthquake. The color scales are different.

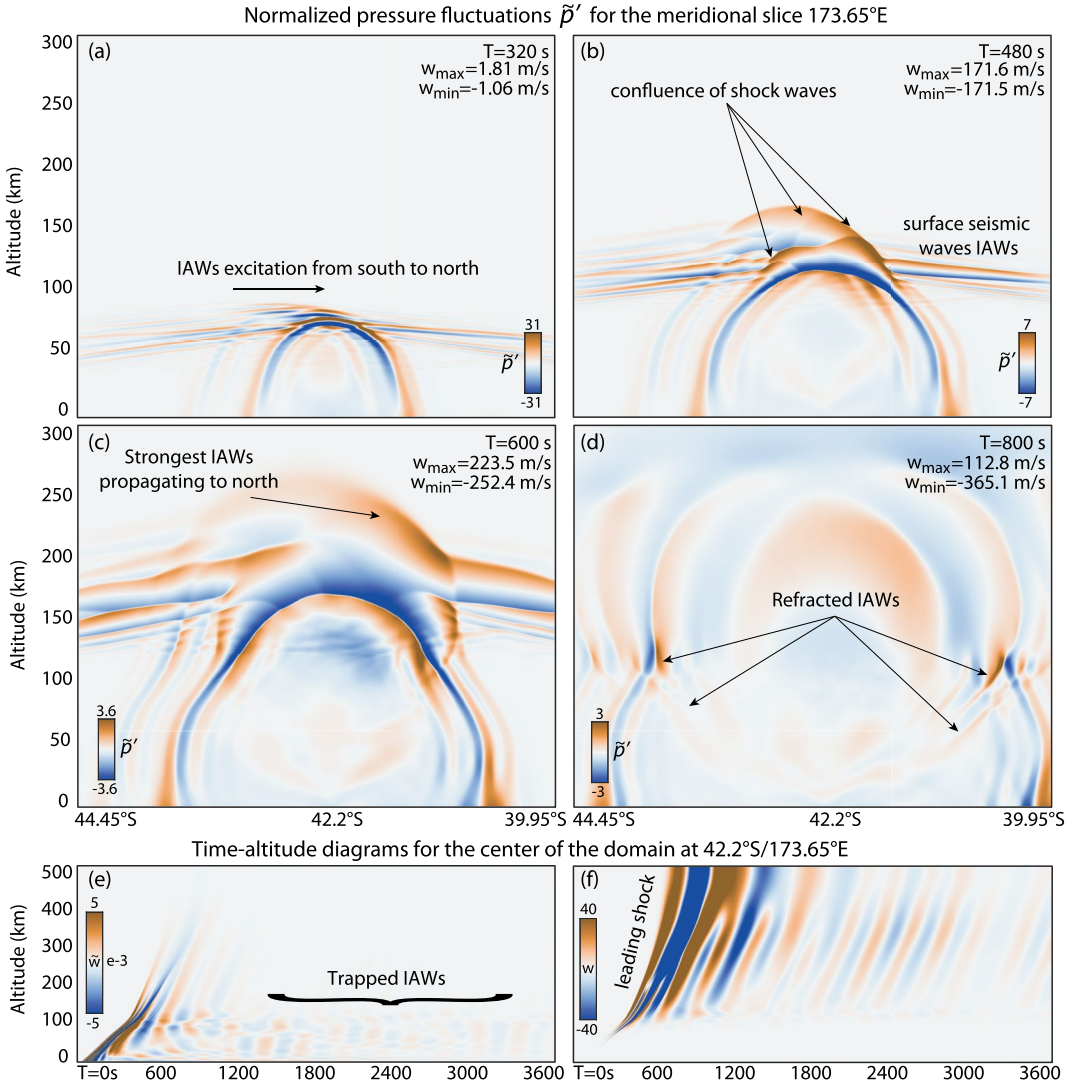

Figure 5. (a–d) Altitude–latitude diagrams of normalized pressure fluctuations ($\tilde{p}'$) for the slice along 173.65°E at four time epochs. Time–altitude diagrams of normalized ($\tilde{w}$) (e) and absolute (f) vertical fluid velocities for the position of Papatea fault (42.2°S/173.65°E). Color scales are oversaturated for better visibility of weak signatures.

from surface seismic wave propagation farther from this area, can be discerned. The complex pattern of IAWs is excited by surface seismic waves and is related to temporally and spatially varying rupture evolution on different faults.

Figures 5a–5d present normalized pressure perturbations ($\tilde{p}' = p' / \sqrt{\rho / \rho_0}$, where p' is the pressure perturbations, ρ is the equilibrium atmospheric density, and ρ_0 is the equilibrium atmospheric density at the ground level) from the atmospheric simulation with Holden–Xu preferred model for the latitude–altitude slice along 173.65°E at four time epochs. The permanent surface deformation drives IAWs starting from the southern faults and later at northern faults (Figure 5a). The IAWs exhibit nonlinearity as they propagate upward from the ground; this includes steepening and the formation of acoustic shocks. The N-wave starts to be discerned from thermospheric heights (>100 km), where individually formed acoustic shocks merge, resulting in a uniform N-wave shock signature reaching ~150 km and higher. Merging of acoustic shocks, generated over northern faults, leads to the strongest IAWs propagating to the north. Their vertical fluid velocities at altitudes 250–300 km peak at +225/−351 m/s (10 s of % of local Mach number, which represents the ratio of fluid velocity to the local speed of sound). The amplitudes of IAWs to the south are comparatively small (Figure 5c).

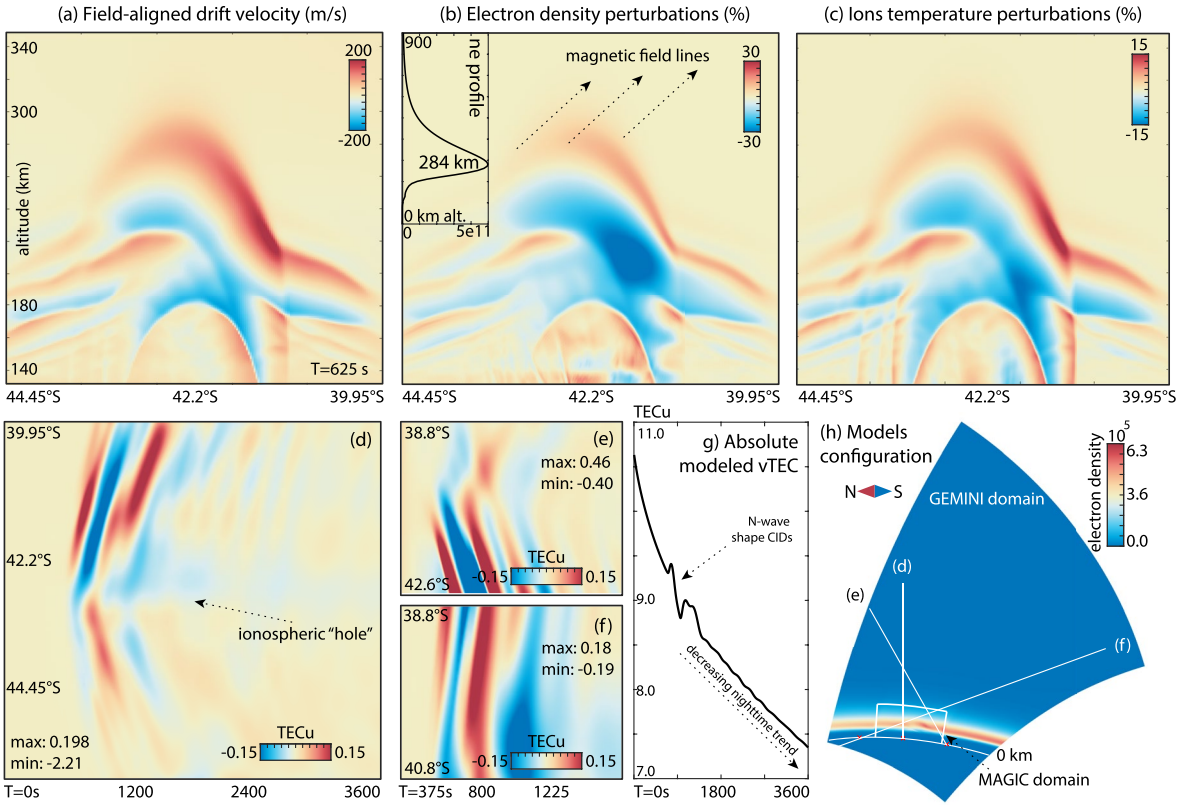

Figure 6. (a) Magnetic field lines-aligned ionospheric plasma velocities, and (b) electron density perturbations and (c) plasma temperature perturbations in percentage from background from simulation with preferred Holden–Xu finite-fault model for the meridional slice along 173.65°E at T_0 + 625 s. (d) Latitude–time diagram of simulated vTEC calculated with zenith integration of electron densities. (e) Latitude–time diagram of vTEC perturbations recalculated from sTEC with 50° elevation angle of LOS pointing to the south. (d) Latitude–time diagram of vTEC perturbations recalculated from sTEC with 30° elevation angle of LOS pointing to the north. The coordinates on diagrams (d)–(f) are specified for IPP positions. Data on plots are oversaturated for better visibility of weak features. (g) Simulated vTEC for the position 173.98°E/40.3°S. (h) Configuration of numerical domains and direction of LOS for latitude–time diagrams shown in panels (d)–(f). Panel (b) contains the profile of electron density for location over the Papatea fault used in simulations. vTEC, vertical total electron content; sTEC, slant total electron content; LOS, line-of-sight; IPP, ionospheric pierce point.

IAWs, generated by surface seismic waves and propagating away from the epicentral area with much faster apparent horizontal phase velocities, can also be discerned as practically horizontal lobes of the wavefield due to large speeds of surface seismic wave propagation (Figures 5a–5c). In the proximity of the epicentral area, their vertical fluid velocities reach amplitudes of ~100 m/s. The direction of the rupture propagation, defining the main lobe of surface seismic wave energy, also results in stronger IAWs to the north and north-east of the epicenter.

Panels e and f of Figure 5 include time–altitude diagrams of normalized ($\tilde{w} = w / \sqrt{\rho / \rho_0}$, where w is the absolute vertical fluid velocity, ρ is the equilibrium atmospheric density, and ρ_0 is the equilibrium atmospheric density at the ground level) and absolute vertical fluid velocities, respectively, at the position of the Papatea fault. Again, the merging of individual acoustic shocks to a single shock N-wave can be seen from ~100 km altitude. Later on, long-lived resonances of IAWs, trapped between lower thermosphere at ~120 km altitude (from partial IAW refraction) and the ground, are present (Godin et al., 2020). They also leak energy to higher altitudes, with a second packet of notable IAWs arriving to ionospheric heights ~30–40 min after the earthquake. IAWs, refracted from the stratospheric heights (~15–30 km), can also be seen (Figure 5e).

To summarize, the modeling results suggest that the strongest IAWs are excited to the north-northeast from the epicentral area. The contributions of comparatively small surface deformations from the southern faults to IAWs to the north-northeast are relatively small. The propagation of IAWs is impacted by nonlinear effects, which lead to the formation of acoustic shocks. At ionospheric heights, acoustic shocks merge to

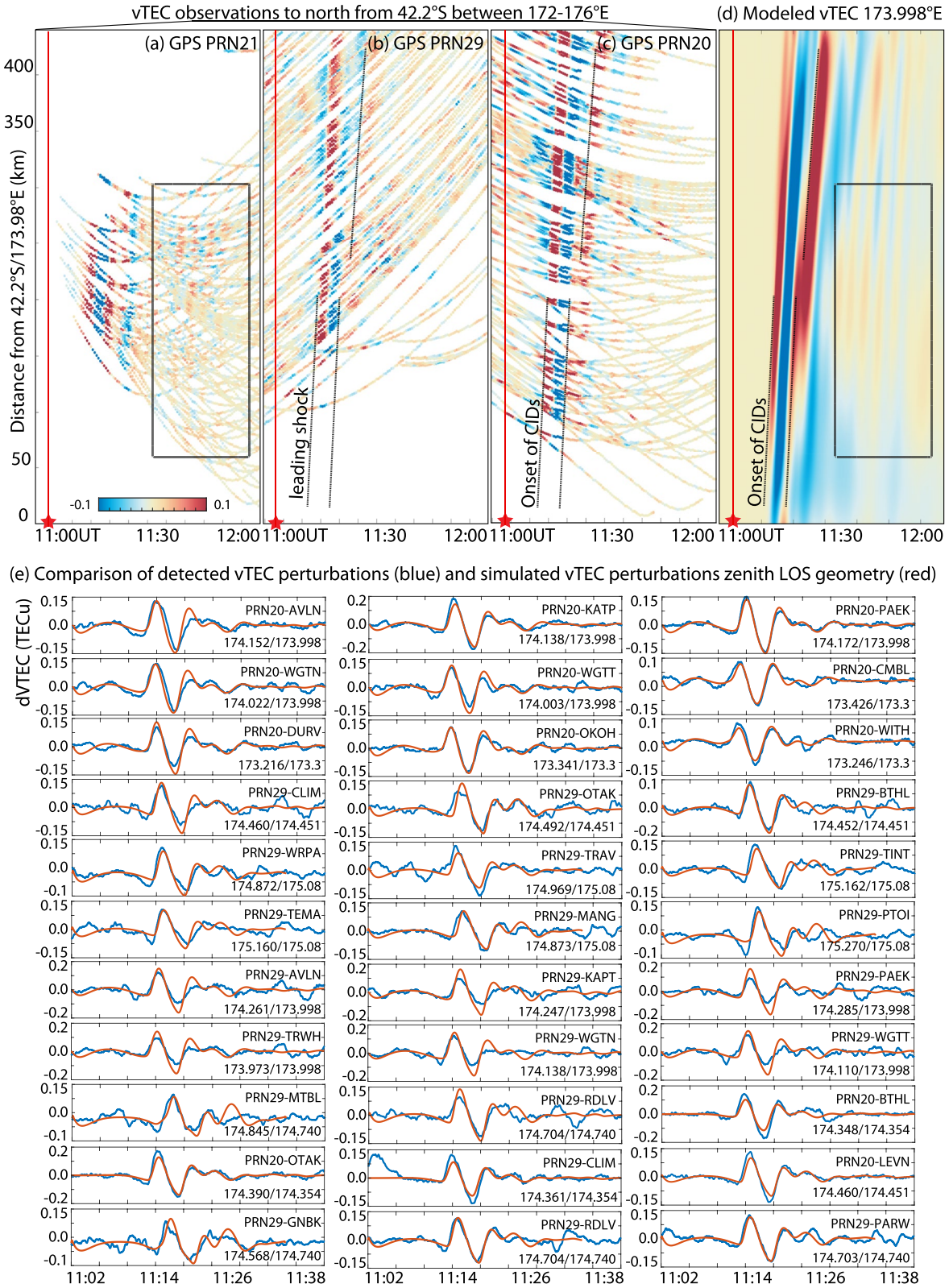

Figure 7. (a–c) Travel time diagrams of 10-s to 8-min band-pass-filtered vTEC to the north from the position of Papatea fault with GPS PRN21, 29, and 20. (d) Travel time diagram of modeled vTEC perturbations for the meridional slice along 173.98°E. (e) Comparison of observed (blue) and simulated (red) vTEC perturbations. Both time series are 20-s to 8-min band pass filtered. vTEC, vertical total electron content.

single N-waves that are then markedly smoothed by dissipation and practically fully damped at 400–500 km altitude. The Papatea fault significantly contributes to the IAWs to the north and northeast.

4.2. Ionospheric Plasma Responses to IAWs

The snapshots from the ionospheric plasma dynamic simulation with the Holden–Xu preferred finite-fault model for the latitude–altitude slice along 173.65°E are presented in Figures 6a–6c. The strongest perturbations in ionospheric plasma are driven by IAWs to the north, and this asymmetry is connected with the dominant plasma motion along magnetic field lines, and with the focusing of the strongest IAWs to the north-northeast, as discussed earlier. Again, we highlight that the fluctuations of plasma at the bottom of ionospheric F-layer driven by IAWs are practically fully constrained along magnetic field lines (supporting our use of 2D ionospheric plasma dynamic model) and thus direction of IAW propagation and the local geometry of magnetic field lines are important. At 250 km and higher, near-epicentral CIDs possess a single (but nonuniform) leading front to the south and north. Surface seismic wave-induced IAWs also drive CIDs farther from the epicentral area, although of comparatively small amplitudes. The propagation of IAWs results in electron density perturbations up to ∼30% from the background unperturbed state, and up to ∼15% in ion (plasma) temperature.

Stronger (weaker) electron density perturbations are generated by surface seismic wave-induced IAWs to the north (south) (Figures 6a–6c). Again, this is driven by two factors: (1) the directivity of rupture propagation that defines the direction of main energy lobe for surface seismic waves and subsequently IAW focusing and (2) longer projection of IAW propagation direction vector along magnetic field lines to the north, whereas for IAWs propagating to the south this vector has smaller projection to magnetic field lines and thus comparatively weak resulting ionospheric plasma fluctuations (Figure 6b).

Panel g of Figure 6 shows the trend of vTEC for the hour after the earthquake at the position 173.98°E/40.3°S. vTEC values match the observations (see Figures 3c–3e) and, in general, we obtain similar values, trends, and gradients of vTEC over the considered region. Simulated vTEC values are ∼9–9.5 TECu in the region of epicentral area, matching observations.

Figure 6 presents latitude–time diagrams of simulated vTEC perturbations using three geometries of LOS: (d) zenith-looking observations, (e) 50° elevation and 180° azimuth angle observations, and (f) 30° elevation and 0° azimuth angles observations. Azimuth angle is set from the north direction and the geometries for one LOS in each case are shown in Figure 6h for reference. We use height of 300 km to calculate IPP coordinates (as for IPP coordinates calculation based on observations) and Single Layer Mapping function to recalculate sTEC to vTEC (Parkinson et al., 1995). The diagram on panel (d) demonstrates latitudinal asymmetry, with stronger TEC perturbations to the north (Figure 6d), as also found in observations. Head (leading) shock of N-waves to the south does not drive significant enhancements in vTEC, whereas their following rarefaction phase, possessing higher amplitudes, generates detectable initial decreases in vTEC. This is also consistent with vTEC observations shown in Figure 3, for example, for PRN20-METH/YALD. For southward-pointing geometry, with LOS practically perpendicular to plasma motion direction at ionospheric heights, as shown in Figure 6h, the mapped vTEC perturbation reaches ∼0.9 TECu ptp, which is almost twice higher than observed with GPS satellites PRN20 and 29 with LOS of 70–85° elevation angles (Figure 6e). The vTEC on panel f is derived from sTEC with LOS geometry practically along plasma motion direction and thus exhibits maximum amplitudes of only ∼0.15 TECu. This illustrates well-known phase canceling effect, as TEC fluctuations tend to be the greatest when TEC LOS lies along CID phase front (Georges & Hooke, 1970). The amplitudes and shapes of simulated TEC perturbations with zenith-looking LOSs show good agreement with TEC observations with GPS satellites PRN20 and 29.

Panels a–d of Figure 7 show time–distance diagrams of filtered vTEC observations with GPS satellites PRN20, 21, and 29 and vTEC perturbations from GEMINI simulation with Holden–Xu preferred finite-fault model. On panels a–c, we show detected vTEC perturbations to the north from the position 42.2°S/173.98°E and 172°E–176°E longitudinal range of IPP positions. Panel d represents simulation results for the slice along 173.98°E from 42.2°S/173.98°E and to 433 km to the north. Black lines are added to each plot to the same positions and times and indicate that apparent horizontal phase speeds of CIDs, and the general dynamics of simulated CIDs are fairly close to those in reality. The N-wave shape of the CIDs for all three

satellite observations and simulation can be seen, and plasma disturbances driven by the head shock of the N-wave have similar apparent phase velocities as in observations—~1.1–1.3 km/s.

Next, we compare time series of synthetic vTEC perturbations with observations. First, the coordinates of IPP positions at the time of leading CID onset (depicted in Figures 6g, 7c and 7d for demonstration) are found from TEC observations. Data are used from GPS satellites PRN20 and 29 only, for which these onsets can be clearly discerned, as for example shown in Figures 3c and 3d. Then, among this data set, we choose observations that are close to the meridional slices to the west and to the east from the epicentral area for which we performed ionospheric simulations. Finally, we use the same latitudes of IPP positions from simulations as found from TEC observations. In summary, we match IPP positions at moments of CID arrivals from observations and simulations and compare vTEC perturbations. For GEMINI simulation, we integrate electron densities vertically (90° elevation angle) to represent zenith TEC LOS, while in observations we use vTEC recalculated from sTEC values with only high (75°–85°) LOS elevation angles. Uncertainties in this methodology are discussed in Section 5.4.

The resulting vTEC perturbation time series comparisons are presented in Figure 7e. For all plots, we indicate the longitudes of CID onsets that are estimated from observations (first value at bottom-right on each plot) and longitudes of meridional slices used from simulations (second value at bottom-right). Overall, we find good agreement with TEC observations, in terms of the timing of CID onsets and their amplitudes and shapes. The latter indicates also a reasonable reproduction of the nonlinearity, present in the observed waveforms, which further supports that the simulated amplitudes of IAWs are reasonable.

Trapped IAWs drive long-lasting CIDs that can be seen from observations and simulation results (e.g., Figures 7a and 7d). Some later-emerging CIDs might have come from early aftershocks (as large as M6.2), although their contributions are expected to be relatively small or negligible. Our results suggest that these long-lasting CIDs must have been driven by trapped IAWs (Figures 5e and 5f), similar to those reported in A. Saito et al. (2011). Reported landslides (Mountjoy et al., 2018), along with ocean dynamics driven by the tsunami (Heidarzadeh & Satake, 2017), are another possible source of atmospheric waves that could potentially contribute to CIDs, although we estimate their effects to be offshore to the east and not in the near-epicentral region we investigate.

Finally, simulation results suggest only very limited formation of an ionospheric "hole," which we define as the decrease in electron density persistent over tens of minutes and driven by a higher rate of ionospheric plasma recombination and quasi-permanent transport of plasma over near-epicentral region (e.g., Astafyeva et al., 2013; Kakinami et al., 2012; Mendillo, 1988; M. D. Zettergren et al., 2017). Its duration is ~20 min and magnitude ~0.03 TECu. We do not find any signatures in TEC observations that can be connected with an ionospheric "hole" with high confidence, particularly because its magnitude is close to the TEC threshold level, which, for the chosen data set, we estimate at the level ~0.02 TECu (see Figure 3).

4.3. Seismo-Ionospheric Imagery

As demonstrated earlier, shock acoustic waves, reaching altitudes of 100–150 km and higher, coalesce into a single N-wave (Figures 3 and 5). Our previous case studies, for the 2015 M7.8 Nepal and the 2011 M9.1 Tohoku-Oki earthquakes, also pointed out similar nonlinear evolution (Inchin, Snively, Williamson, et al., 2020; Inchin, Snively, Zettergren, et al., 2020). Such common dynamics resemble, for example, the confluence of acoustic shocks excited by supersonic aircraft: while shock-wave signatures at close to aircraft distances depend on the source parameters, at sufficiently far distances, which depend on the characteristics of initial signal, they coalesce into N-wave (Carlson et al., 1966). Thus, in a homogeneous atmosphere, the resulting long-time behavior shape at far field does not depend on the source characteristics (Carlson & Maglieri, 1972; Smoller, 2012). However, the durations, amplitudes, and times of arrival of the resulting N-waves at far distances do depend on the source characteristics (Howes, 1967; T.-P. Liu, 1977). In general, however, the shape of N-waves may be distorted by atmospheric stratification, winds, and turbulence (Crow, 1969; Marchiano et al., 2005; Pierce & Maglieri, 1972; Sabatini, Snively, et al., 2019), as well as nonlinear effects and wave focusing (Inoue & Yano, 1997; Sabatini, Marsden, et al., 2019). Also, for earthquakes, the dynamics are complicated by the initial formation of acoustic shocks that may evolve at different altitudes due to the spatial and temporal variability of IAW sources.

Table 1
Finite-Fault Models and Configuration of the Papatea Fault Used in the Analysis

Model	Papatea fault nucleation time (s)	Papatea fault rupture propagation direction
1. Preferred Holden–Xu	T_0 + 57	From south to north
2. Holden et al. (2017)	N/A	N/A
3. Wang et al. (2018)	T_0 + 27	From northwest to southeast
4. Holden–Xu	T_0 + 27	From south to north
5. Holden–Xu	T_0 + 27	From northwest to southeast
6. Holden–Xu	T_0 + 57	From northwest to southeast
7. Holden–Xu	T_0 + 57	From north to south

Note. T_0 is the origin time of the earthquake.

Thus, we propose that the earthquake rupture process must influence the characteristics of the N-wave(s) reaching the ionosphere, and their generated CIDs and subsequent variations in times of arrivals, amplitudes, and periods of TEC perturbations. Such inference must be carefully interpreted on a nonlinear basis—for example, assessing amplitudes and time of arrivals of the nonlinearly evolved wavefield, with an appreciation that they have evolved from their initial forms.

4.3.1. Comparison of IAWs and CIDs From Various Models

In order to understand the sensitivity of TEC perturbations to earthquake evolution parameters, we consider seven finite-fault models, which vary in their specification of rupture progression on the Papatea fault (Table 1). With these models, we investigate (1) if Papatea fault was ruptured during the Kaikoura earthquake, (2) time of rupture initiation on the Papatea fault, and (3) direction of rupture propagation on the Papatea fault. For example, in the finite-fault model of Wang et al. (2018), the rupture on the Papatea fault initiates at the northwest of the fault at ∼27 s after T_0 and propagates toward the southeast. Hence, the timing of the Papatea fault rupture in this model is 30 s earlier with respect to our preferred Holden–Xu model, described in Section 3. In each case, we run seismic wave propagation, atmospheric and ionospheric simulations as described in Section 3.

Figure 8 presents snapshots of atmospheric vertical fluid (flow) velocities and ionospheric electron density perturbations for the meridional slice along 173.98°E for two time epochs from simulations with finite-fault Models 1–3 and 5, as well normalized atmospheric pressure signals at two altitudes (150 and 250 km). Resulting IAW and CIDs are compared for the region of maximum contribution of the Papatea fault to the north and northeast, in the same manner as discussed previously. The results with other models are presented in the Supporting Information.

Simultaneous rupture on northern faults in Model 1 leads to a stronger N-wave before reaching the altitudes where wave damping from thermo-viscous dissipation becomes dominant, thus resulting in stronger CIDs (Figure 8a and 8m). However, in the case of earlier rupture initiation on the Papatea fault (i.e., Models 3–5), the confluence of acoustic shocks does not form a uniform N-wave until ∼230 km, where dissipative damping is already substantial, finally resulting in weaker CIDs for Models 3–5 (panels c, d, g, h, and m in Figure 8). At 150 km altitude, pressure signals exhibit separate leading shocks in these cases (Figure 8m); and although reaching 250 km pure N-wave is formed, its amplitude is substantially lower than in simulation with Model 1. Simulations with Models 3–5 show similar IAW wavefields and pressure signals at ionospheric heights to the north and northeast. We find that simulations with Holden–Xu Models 4 and 5 (i.e., earlier Papatea fault rupture initiation) show 20% and 25% lower amplitudes of vertical fluid velocities of IAWs in the bottom F-layer of the ionosphere than in simulation with Model 1.

We further explore the influence of rupture propagation direction on the resulting IAW amplitudes and TEC perturbations. From Models 6 and 7, we find that the Papatea fault rupture propagation direction affects IAW amplitudes to the north and northeast, but only to ∼7%–10% in vertical fluid velocities. Thus, taking into account possible uncertainties in the determination of initial atmospheric and ionospheric states and model configurations (Section 5.4), it is difficult to draw any strong conclusions on the Papatea fault rupture propagation direction, at least with 2D simulations and proposed comparison approach of simulated vTEC with high-elevation TEC LOS observations. The difficulties are exacerbated by the fact that large vertical surface deformation occurred at two areas over the main Papatea fault strand: (1) at its northern end and (2) to the southeast, near the shore (Figure 2d) (see e.g., Diederichs et al., 2019; Langridge et al., 2018), resulting in a complex pattern of excited IAWs in the atmosphere.

Finally, Model 2 (i.e., excluding the Papatea fault) shows practically uniform N-wave at 150 km that exhibits ∼35% smaller amplitudes than in simulation with Model 1. Also, its leading shock reaches ionospheric altitudes notably later than in other simulations (Figure 8f).

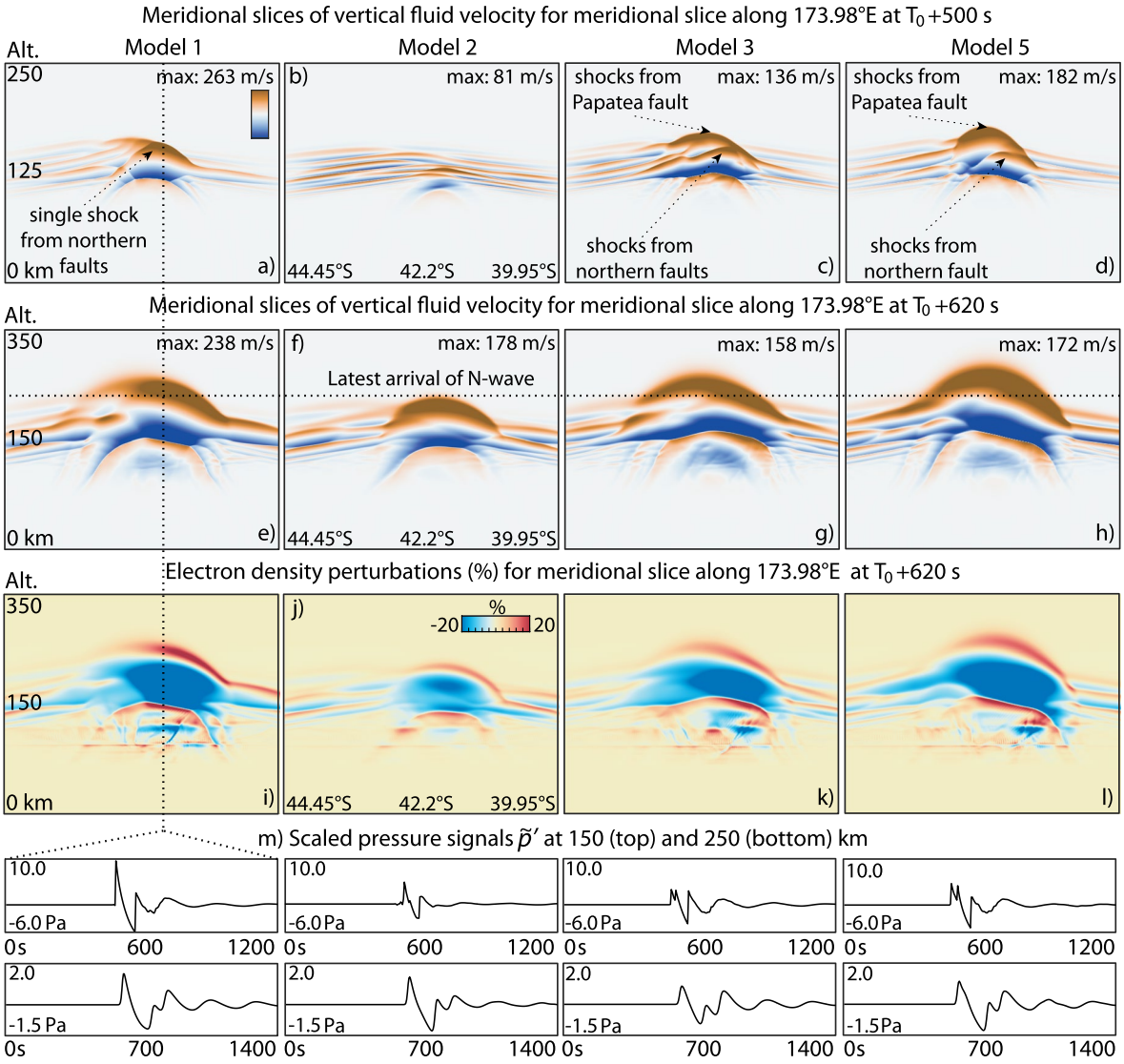

Figure 8. Latitude–altitude diagrams of vertical fluid velocity for the meridional slice along 173.98°E from simulations with Models 1–3 and 5 at (a–d) $T = 500$ s and (e–h) $T = 620$ s. (i–l) Electron density perturbations for the same models as above at $T = 620$ s. (m) Normalized pressure signals at 150 and 250 km for the position 42.08°S/173.98°E (along dashes lines though plots (a) and (e)). Color scales at plots (a)–(h) are oversaturated by 1.5 times for better visibility of weak signatures and absolute maximum velocities are provided for each plot instead.

In summary, these results demonstrate that IAWs are sensitive to the time of the Papatea fault rupture initiation (or to the absence of the Papatea fault) and amplitude differences vary in the range of ~20%–35%. In all cases, we find practically the same differences of CID amplitudes (in percent from the background) as of IAW amplitudes: the strongest CIDs are simulated with Model 1, weaker with Models 3 and 5, and fairly weak with Model 2 (Figures 8i–8l). As Models 4 and 5 and 1, 6, and 7 showed small differences in IAW amplitudes (~5% and ~7%–10%, respectively), further in the text we discuss modeling results only based on Models 1–3 and 5, which demonstrate substantial differences and thus allow providing conclusive outcomes.

4.3.2. Comparison of TEC Signals

Figure 9a presents the comparison of simulated TEC signals based on earthquake finite-fault Models 1–3 with high elevation angle LOS TEC observations to the north and northeast. Simulated TEC perturbations based on Model 3 show, on average, 38%–40% lower amplitudes than from simulation with Model 1 or observations. The absence of the Papatea fault in Model 2 shows ~30% lower amplitudes of TEC perturbations

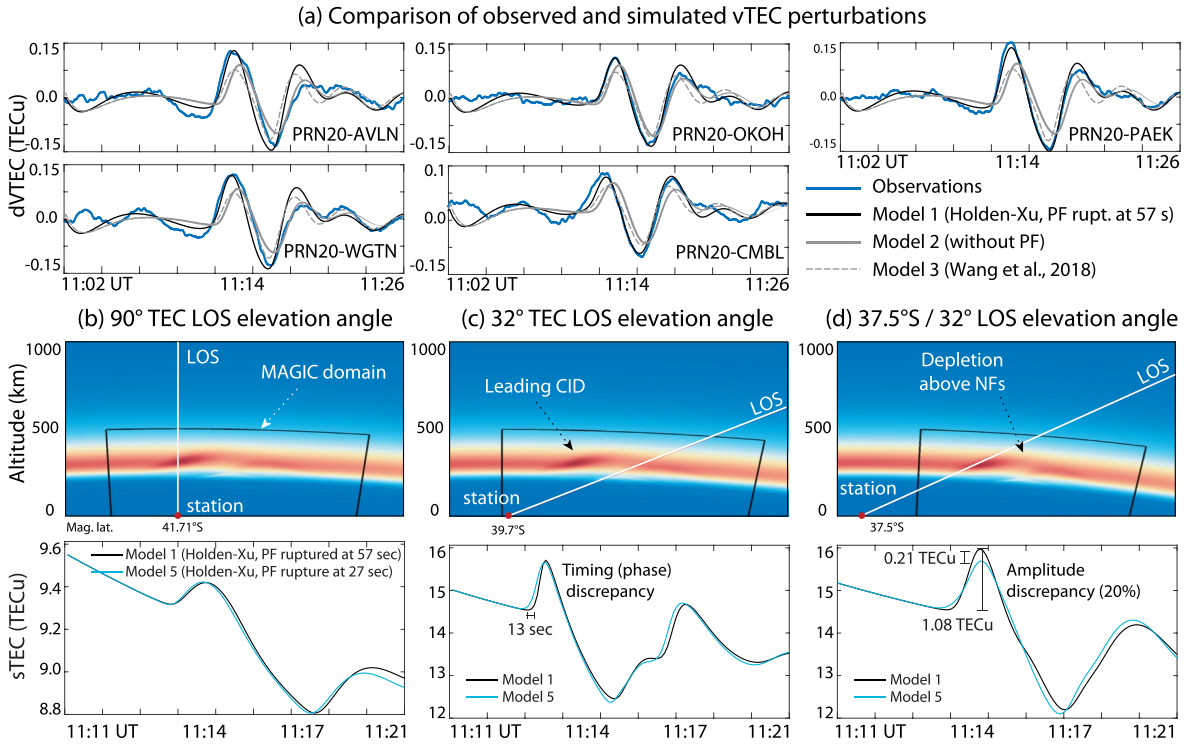

Figure 9. (a) Comparison of observed and simulated TEC perturbations based on Model 1 (Holden–Xu with the Papatea fault ruptured at 57 s), Model 2 (Holden et al., 2017, without the Papatea fault), and Model 3 (Wang et al., 2018) to the north and northeast from the focal area. (b–d) Comparison of TEC perturbations between Model 1 (black) and Model 5 (Holden–Xu with the Papatea fault ruptured at 27 s, cyan) in three LOS geometry of TEC observations. TEC, total electron content; LOS, line-of-sight.

and later (tens of seconds) arrivals of CIDs than detected with observations. These systematic biases in simulation with Model 2 are found for the majority of TEC observations in the considered near-epicentral region to the north and northeast, suggesting the need of incorporation of the Papatea fault rupture during the earthquake.

At the same time, amplitudes of TEC perturbation with Model 5 are practically the same as with Model 1 (Figure 9a). This shows that, due to phase canceling effect, TEC measurements, as integrated values through wave structures (resulting from IAW propagation), may be less sensitive to differences in CIDs, although IAW and CID amplitudes are ~20%–25% weaker in simulation with Model 5 than in Model 1. To demonstrate this phase cancellation effect, we compare sTEC from simulations with Models 1 and 5 with different geometries of LOS in Figures 9b–9d. Zenith-looking TEC observations show practically no useful difference in perturbations (Figure 9b); however, the slant geometry of TEC observation (50° elevation angle) demonstrates both differences in time of CID arrivals and their amplitudes (Figures 9c and 9d). As shown in Section 4, the IPP position and spatial configuration of LOS relative to the direction of plasma motion play an important role in the detection of CIDs. When CID intersects LOS at altitudes ~250 km, as shown in Figure 9c, TEC amplitude differences between two simulations are negligible, but TEC remains sensitive to the time of CID appearance (~13 s). In case where plasma motion intersects LOS at altitudes ~300 km, the difference in time of CID appearance is negligible, but amplitudes differ by ~20% (Figure 9d).

5. Discussion

5.1. Apparent Propagation Velocities of CIDs

For the 2016 M7.8 Kaikoura earthquake, Bagiya et al. (2018) and Lee et al. (2018) reported apparent horizontal phase speeds of CIDs as 1.05–1.4 km/s based on TEC observations. They pointed that the values exceed the speed of sound of IAWs in the F-layer of the ionosphere that drive these CIDs. In addition, Lee et al. (2018) concluded that travel time delays in their simulated TEC waveforms, based on linear IAW

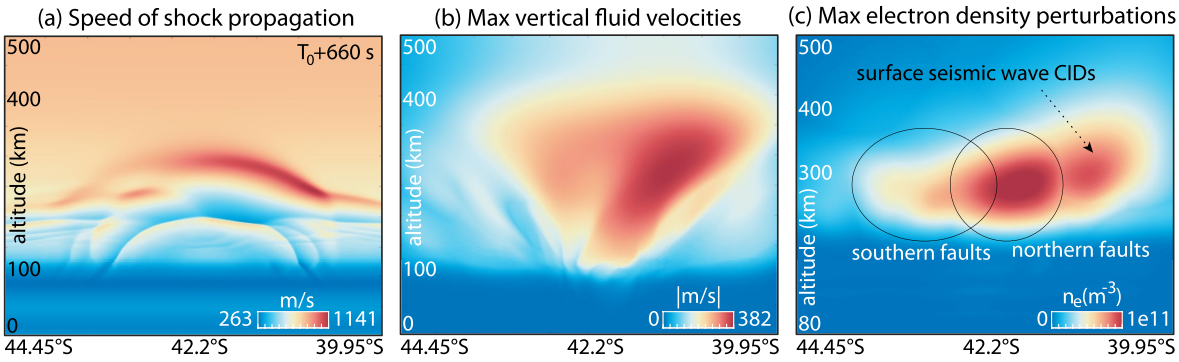

Figure 10. (a) Speed of shocks relative summed up with speed of sound for each point for the meridional slice along 173.98°E at $T = 660$ s. (b) Wavefield of maximum absolute vertical fluid velocities for the full hour of simulation for the meridional slice along 173.98°E. (c) Field of maximum electron density perturbations calculated for the full hour of the simulation for the meridional slice along 173.98°E. The results are based on simulation with Preferred Holden–Xu finite-fault model.

propagation approximations, may be related to the errors in a wind model used. Although this conclusion may be valid, we propose other reasons for higher apparent speeds of CIDs. First, the curvature of the IAW phase fronts relative to TEC LOS and inhomogeneities in ionospheric plasma distribution may result in apparent variations of horizontal phase velocities calculated from vTEC observations. We expect that these effects produce small impacts, as dozens of TEC observations are available for the considered event with different geometry of LOS and IPP coordinates to investigate phase velocities.

Second, this can be explained by the nonlinear propagation of IAWs. In addition to the substantial increase of the mean atmospheric temperature at altitudes above ~120 km, which leads to higher speeds of sound, the faster speed of propagation of the head shock of N-wave (and slower speed of propagation of its tail shock) leads to the lengthening of the N-wave pulse (Whitham, 1974). The present case study corroborates our previous findings of the formation of a single N-wave reaching the upper atmosphere, based on case studies of the 2015 M7.8 Nepal and the 2011 M9.1 Tohoku-Oki earthquakes (Inchin, Snively, Williamson, et al., 2020; Inchin, Snively, Zettergren, et al., 2020), which also support the conclusions of numerous observational studies (e.g., Afraimovich et al., 2001; Astafyeva et al., 2009; Reddy et al., 2017). Within the weakly nonlinear regime (when IAW amplitudes are below ~1/10 of local atmospheric pressure), the speed of both head and tail shocks of N-wave relative to the center of N-wave can be found as $v = \phi c_0(\gamma + 1)/2\gamma$, where $\phi = p/p_0 - 1$, γ is the adiabatic index, c_0 is the local speed of sound, and p and p_0 are disturbed and equilibrium pressures, respectively (e.g., Beyer, 1974). Thus, for nonnegligible pressure changes, the speed of the head shock of N-wave always exceeds the speed of sound, the tail shock lags, whereas center point of N-wave (point of zero fluid velocity) propagates with the speed of sound.

We provide the diagram of shock speeds calculated based on the formula above and estimated using the local mean speeds of sound for every point of the numerical domain for the meridional slice along 173.98°E at $T_0 + 660$ s, when the head shock of N-wave is in the F-layer of the ionosphere (Figure 10a). The results are based on simulation with the preferred Holden–Xu model. As the provided formula neglects terms of order $\phi^2 + O$ (along with consideration of plane wave propagation in a homogeneous fluid without wind), we still obtain close values of head shock speed as from our numerical simulation—1.141 km/s versus ~1.1–1.3 km/s. It is important to highlight that the consistencies in times of CID arrivals from simulation with preferred Holden–Xu finite-fault and TEC observations support our conclusions.

In addition, at ionospheric heights, larger amplitudes of the formed N-wave result in stronger distortions of its shape (Figure 8m). Particularly, the curvature of the central part of the pressure signal is seen from the results with Model 1, where maximum amplitudes of N-wave are simulated. For Model 2, the central part of N-wave exhibits only slight distortion, whereas N-wave possesses practically straight central part with Models 3 and 5. This may be due to the strongly nonlinear propagation of IAWs, and the importance of higher order effects in p/p_0, where p is the pressure and p_0 is the equilibrium pressure (Sabatini, Marsden, et al., 2019).

5.2. The Importance of Finite Characteristics of Coseismic IAW Sources

Bagiya et al. (2018) proposed that the separation between various tectonic sources of IAWs near the epicenter within rupture duration of ~100 s may not be possible and explained this by the much shorter time of rupture propagation in comparison with periods of CIDs (~4 min). Our current study demonstrates the importance of the directivity of rupture propagation to resulted IAW wavefield, even at ionospheric heights. In addition to the results presented in Figures 4, Figure 10b presents the field of maximum absolute vertical fluid velocities, reached at each point for the latitude–altitude slice along 173.98°E and Figure 10c—maximum reached electron density perturbations for the same slice. These maximum values are derived considering the dynamics for the whole hour after the earthquake. The IAW wavefield exhibits a meridionally asymmetric pattern due to the finite nature of the source and north-northeast direction of rupture propagation. The strongest perturbations are driven by IAWs to the north, with weaker perturbations to the south and above southern faults. IAWs exhibit the strongest fluid velocities at 250–300 km, with a substantial decrease of amplitudes at higher altitudes driven by thermo-viscous dissipation. A similar spatial pattern can be seen in the maximum electron density perturbation field; the strongest perturbations were driven to the north at ~280–310 km, which supports our choice of 300 km altitude for the calculation of IPP coordinates.

Earlier, based on modeling results of atmospheric and ionospheric responses for the 2015 M7.8 Nepal Gorkha earthquake, we also demonstrated that the direction of rupture propagation, as a supersonic moving source of IAWs in the atmosphere, defines the direction of IAW focusing, notable even at ionospheric altitudes (Inchin, Snively, Zettergren, et al., 2020) and these outcomes were supported by observational studies based on TEC (Catherine et al., 2017; Sunil et al., 2017). In the case of simpler, unilateral rupture over a much longer fault length, as in the Gorkha earthquake, strong correlation between the direction of rupture propagation and propagation of the strongest IAWs is present. Also, CIDs of 4–6 min periods in the ionosphere may results not only from IAWs of same periods as excited at the surface but also from nonlinear effects on IAW propagation that lead to the formation of N-waves, followed by their lengthening and subsequent smoothing at ionospheric altitudes by thermo-viscous damping, as discussed above.

Thus, in addition to complex plasma responses to atmospheric waves (magnetic field-seized plasma mobility and plasma distribution), we highlight that source effects also play a vital role in ionospheric arrivals of IAWs. The need to consider finite-faulting processes for large earthquakes at near-epicentral regions is dictated not only by seismological principles but also by spatial asymmetry of IAWs in the atmosphere.

5.3. Investigation of Earthquake Evolution "From Above"

The analysis provided in Section 4.3 indicates the need for the inclusion of the Papatea fault into finite-fault model to reproduce detected TEC perturbations and therefore suggests that the Papatea fault was ruptured during the Kaikoura earthquake. We found that the absence of the Papatea fault results in a substantially lower amplitudes of simulated TEC perturbations (~30%). Providing further support for the significance of this result, temporal lags in the appearance of simulated TEC perturbations, in case of the absence of the Papatea fault (tens of seconds), serves as an additional confirmation for the necessity of the Papatea fault to reproduce the dynamics of IAWs and their nonlinear evolution. Specifically, the presence of the Papatea fault markedly increases amplitudes of formed N-wave and its lengthening, which results in earlier arrival of its head (leading) shocks to ionospheric heights. The weakest perturbations in the source model by Wang et al. (2018) are caused by lower amplitudes of surface deformation and differences in the rupture kinematics, although, as we demonstrated, similar IAW and CID dynamics to the north-northeast can be obtained by reconfiguring the Papatea fault rupturing process in the Holden–Xu finite-fault model (Model 5).

The full sensitivity analysis of the rupture kinematics of the Papatea fault, including direction of rupture propagation, would require full 3D ionospheric simulations. Particularly, with the precise tracking of LOS and the use of low elevation angle sTEC observations (GPS satellites PRN05, 21, and 29), it is plausible that further steps toward resolving the Papatea fault rupture can be made. Further investigation may be warranted to understand the sensitivity of conditions of atmosphere and ionosphere on a statistical basis through numerical parametric studies. We would like to highlight that these numerical simulations are very computationally expensive, and parametric studies, as shown here, already require hundreds of thousands

of core-hours of calculations on a high-performance computing cluster. However, with the improvement of models and computational resources, such parametric studies may soon become feasible.

These findings call for the need for denser networks of ground-based receivers and the inclusion of TEC measurements based on signals from other constellations of navigational satellites, for example GLONASS, BeiDou, and Galileo (Ren et al., 2016; Savastano et al., 2019), as well as the more widespread use of other observational techniques and instrumentation. Among them are atmospheric and ionospheric airglow imagers (Pilger et al., 2013; Inchin, Snively, Williamson, et al., 2020), ionosondes (Chum et al., 2012; Maruyama et al., 2017), RADAR and LIDAR systems (Occhipinti et al., 2018), magnetic field observations, etc. The use of radio-occultation observations and satellite missions that deliver information on atmospheric and ionospheric states (such as NASA TIMED, GOLD, and ICON) may also provide additional constraints on simulations of ambient ionospheric conditions to improve precision.

Finally, the small amplitude of the simulated electron density depletion ("ionospheric hole"), as discussed in Section 4.2, may lead to difficulties with its detection, as it can be obscured by other dynamics. This raises an important question of ionospheric "hole" observation applicability for tsunami early-warning systems proposed by Kamogawa et al. (2016), particularly during nighttime events, when the density of ionospheric plasma is low. Although the surface uplift is substantial (up to ∼4–10 m over ∼30 × 30 km region) and results in strongly nonlinear IAWs, the simulated ionospheric "hole" is still fairly weak and at the level of TEC threshold of detectability. We recall that electron density depletion is not found in available TEC observations too.

5.4. Possible Sources of Uncertainties

In this subsection, we discuss possible sources of uncertainties in the data sets and models used, and their configurations, as they can contribute uncertainties that play important roles in interpretation of the dynamics in different media.

In Section 2, we have addressed the questions of uncertainties in the model parameters by considering different finite-fault kinematics. Since the Kaikoura earthquake was a complex event, we cannot explore the full parameter space to address the uncertainties in the finite-fault kinematics due to computational limitations. For example, in both Holden and preferred Holden–Xu models, the deformation is slightly overestimated in general, because the final slip distributions were previously obtained assuming a homogeneous elastic half-space (Clark et al., 2017; Xu et al., 2018), as opposed to a 3D velocity model accounting for lower rigidity rocks at shallow depths assumed in our simulations (see Supporting Information). One example of major uncertainties is whether there was a large (>5 m) slip on the Hikurangi subduction interface. Unlike the preferred Holden–Xu model, the broad uplift around the northern faults (Figure 2c) might be a signature of major slip on the subduction interface (e.g., Wang et al., 2018). In contrast, all the published studies reported the presence of large crustal uplift associated with the Papatea fault rupture (Figure 2c), which is a robust feature. Since the timing (and even its coseismic rupturing) and propagation direction of rupture on Papatea Fault was not well constrained by traditional, seismic and geodetic data sets, our study has focused on this issue.

Currently, MAGIC does not include topography, incorporating a flat bottom boundary that represents Earth's surface. The topography in the region considered varies between 0 km (near the ocean) and 2 km. Such variations can result in maximum 6 s difference in the arrival of IAWs to the certain altitude. We assume these discrepancies to be negligible for the investigation of long-range IAW propagation (284 km toward the peak of electron density in F-layer of ionosphere in ∼600 s), taking into account other possible uncertainties in the profiling of atmosphere, winds, and timing of IAW sources, as well as resolution of the neutral atmosphere model domain. In addition, the area of main vertical surface displacements is localized around the Papatea and Kekerengu faults, providing negligible differences in timing of IAW excitation from the topography. We note that the topography was included to the simulation of seismic wave propagation, incorporating its effects on seismic wave dynamics and thus vertical displacements.

For the precise comparison of TEC observations with simulation results, we would need 3D ionospheric simulations and to track every GPS satellite-receiver LOS, accounting for the change in their elevation and azimuth angles temporally. Thus, in our comparison, some biases are expected later in time, because

we match only positions of CID onsets with fixed meridional slices from simulations; in reality, IPP positions are constantly moving. Also, the periods of CIDs may be biased from Doppler shift effects (caused by IPP motion relative to CIDs propagation), while our simulation results are free from this effect due to the assumptions of frozen LOS. Another source of possible inconsistency is the effect of mutual geometry between the CID propagation direction and the LOS that may differ in simulation and in reality, as discussed in Section 4.2. These inconsistencies are assumed to be small for chosen observations with high elevation angles of LOS (75°–85°), that possess comparatively negligibly slow speeds of IPPs (Savastano, 2018). In addition, IPP positions can be offset, as we do not know the exact vertical electron density profiles for each location. However, at ionospheric altitudes IAW wavelengths are ∼100–160 km and speeds (∼1.1 km/s), relative to the slow motion of IPPs or small-scale ionospheric plasma irregularities. Thus, we assume that, for the comparison of leading IAWs and the CIDs driven by them with high elevation angle vTEC observations, our approach is sufficient and, likely, as good as feasible without performing a fully 3D GEMINI simulation. We estimate the error in the determination of vTEC to be in the range ±1 TECu and accuracy of ∼0.02 TECu.

Another potential source of uncertainties is the ambient atmospheric density. Note that a 43% increase in amplitude (factor 1.43 to compensate for a 30% deficit) could be attributed to a neutral mass density ∼49% (factor ∼0.49) of that estimated by empirical model NRLMSISE00 near the IPP altitude at 300 km (assuming linearity) and this deviation appears unlikely. Likewise, the sensitivity of IAW amplitude to nonlinear evolution as they propagate upward should be further-quantified; however, most conceivable scenarios lead to weaker rather than stronger IAWs and responses. Also, we found that to reach to the amplitudes of the detected TEC perturbations in our simulations without the incorporation of the Papatea fault, the background electron density would need to have been much in vTEC than found in observations. For comparison, we run two simulations with vTEC in the region of interest with ∼13 TECu and ∼14.5 TECu, that were obtained from GEMINI simulations 1.7 and 5.7 h prior to the earthquake, in the local evening and day times, when ionospheric plasma density is higher due to solar radiation impacts. The results of comparison of TEC perturbations from simulations using earlier initial ionospheric plasma conditions with observations are provided in the Supporting Information. In these simulations, we indeed find amplitude increase of TEC perturbations but that remained insufficient to replicate observed perturbations. The amplitudes of TEC perturbations in ionospheric state of 14.5 TECu show only very limited increase in comparison with 13 TECu case. To recall, values of vTEC from available receivers were found to be 9.5 TECu over the epicentral region and they match simulation results. Meanwhile, no vTEC of 13 (∼36% higher) or 14.5 TECu (∼50% higher) were found in available observations with all receivers during the earthquake. Moreover, substantial lags of CID onsets in these simulations are still present and cannot be eliminated, requiring some other physical reasoning.

Severe geomagnetic conditions, for example during geomagnetic storms, may also impact resulting profiles and gradients in ionospheric plasma densities. However, during the Kaikoura earthquake Kp index was 3 and Dst index −20 nT, which are consistent with quiet geomagnetic conditions. Disagreements between simulated and measured shapes and the altitudes of peaks of electron density profiles can provide additional biases. Thus, we compared the electron density profile from our simulations (presented in Figure 6b) and the profile of electron density from radio-occultation measurements registered with COSMIC satellite at 10:55 UT (7 min prior to the earthquake) to the east from South Island of New Zealand (figure is provided in the Supporting Information). It can be seen, that the altitudes of the peak of electron density in observations (∼288 km) and peak of electron density from simulations (∼284 km) match closely, indicating accuracy of simulations of electron density distribution.

The combination of ∼30% lower amplitudes of TEC perturbations and later times of CID arrivals (phase lags in TEC) in the simulation with the Holden–Xu model excluding the Papatea fault can most plausibly be explained by weaker IAWs generated from the ground and then comparatively small lengthening of formed N-wave. Thus, the simulations favorably support that the amplitude and timing of the signals are consistent with additional surface motions that can be explained by the hypothesized Papatea fault rupture.

6. Conclusion and Future Work

Through simulations using physics-based numerical models, we investigated the dynamics of IAWs generated by the 2016 M7.8 Kaikoura earthquake and their corresponding disturbances in the ionospheric plasma. We simulated time-dependent surface deformation using the forward seismic wave propagation code SPECFEM3D, which was used to drive the 3D nonlinear compressible neutral atmosphere model MAGIC. Plasma responses, excited by the seismically induced IAWs, were then simulated with the 2D nonlinear multispecies ionospheric plasma dynamic model GEMINI.

Specifically, we investigated the contribution of different faults, involved in the earthquake rupturing process, to atmospheric and ionospheric signals through the use of different configurations of the Holden–Xu finite-fault model. We found that our preferred finite-fault model, that includes rupture on the Papatea fault during the earthquake, reproduces the amplitudes, shapes, and time epochs of appearance of detected TEC perturbations most accurately. The absence of the Papatea fault showed significant ∼30% lower amplitudes of TEC perturbations, as well as significant timing (phase) differences, supporting the interpretation that the Papatea fault was ruptured within the coseismic phase of the earthquake.

To investigate further, we then varied the timing of rupture initiation on the Papatea fault and its rupture propagation direction and demonstrated that these parameters result in differences of amplitudes of IAWs reaching ionospheric heights and corresponding CIDs. However, for chosen high elevation angle observations, used for the comparison with 2D ionospheric plasma dynamic simulation results, vTEC was found to be insufficiently sensitive to these kinematic source characteristics. Nevertheless, in case of the 3D ionospheric simulations and precise tracking of satellite-to-receiver LOS of sTEC perturbations, the timing and the direction of the Papatea fault rupture could potentially be further constrained. Thus, we find substantial justification and opportunity for future fully 3D sTEC simulations to investigate seismically generated IAW fields toward reconstructing earthquake processes.

We highlight the following general conclusions as well:

1. For the simulation of IAW excitation and subsequent CIDs from the earthquake's source region, finite-fault models should be considered, particularly for complex events. Rupture propagation (and its direction) plays an important role in the spatial asymmetry of observed CIDs and can be assessed separately from observational biases imposed by the geomagnetic field and with reasonable consideration for atmospheric variability.
2. The regime of propagation of IAWs, driven by large earthquakes, can be weakly to strongly nonlinear, leading to substantially different dynamics in comparison with linear assumptions. In this case, direct physics-based numerical simulations are the most comprehensive way to resolve IAW propagation through the whole range of altitudes and to subsequently reproduce accurate CIDs.
3. Trapped IAWs occur between ∼120 km altitude and the ground, leaking some part of their energy into the ionosphere, and can drive long-appearing CIDs, observable in TEC even an hour after the event. This supports prior investigations, for example, by Matsumura et al. (2011) and M. D. Zettergren et al. (2017).
4. TEC observations may supplement seismological studies through the investigation of different earthquake finite-fault models and their ability to reproduce detected ionospheric perturbations. These findings may be particularly relevant for large undersea earthquakes with lack of geophysical and near-field data.
5. TEC observations (as they are integrated spatially along specific LOSs between GPS satellite and ground-based receiver) are affected by the geometry of LOS and plasma motion direction. Thus, TEC, in a particular geometry of LOS, may be insufficiently sensitive to the differences in amplitudes of electron density perturbation. For such studies, the analysis of vTEC perturbations presented here can be improved by tracking TEC LOS precisely and comparing time of CID arrival and their amplitudes based on sTEC observations.

It is anticipated that modeling and parametric case studies based on full 3D-coupled atmosphere–ionosphere modeling, as well as full sTEC reconstructions, can provide additional insights on earthquake–atmosphere–ionosphere processes. Such simulations, though currently computationally intensive, may provide a significant path forward to constrain finite-fault models of large earthquakes, especially for complex events.

Data Availability Statement

Radio-occultation data, shown in the Supporting Information, are freely available here: https://cdaac-www.cosmic.ucar.edu/. SPECFEM3D-Cartesian code are available through https://geodynamics.org/. Ionospheric plasma dynamics model GEMINI is available through its GitHub repository. Detailed movies of the simulations and relevant data in support of reproducibility can be found here: https://commons.erau.edu/dm-earthquake-acoustic-impacts-ionosphere/.

Acknowledgments
This research was supported by NASA grants 80NSSC18K1037 and 80NSSC20K0495 to ERAU and a Rutherford Discovery Fellowship provided by the Royal Society of New Zealand. Portions of this work were performed at the JPL, California Institute of Technology, under a contract with NASA. We acknowledge the New Zealand GeoNet project and its sponsors EQC, GNS Science, and LINZ, for providing GPS data used in this study, freely available through https://www.geonet.org.nz/. We thank Ian Hamling for providing us the vertical displacement field derived from SAR azimuth and range offsets. We thank Jaime Aguilar for providing numerical tools for calculation of sTEC and vTEC based on simulation results. We also thank Mala Bagiya, Roberto Sabatini, and Byron Iijima, as well as reviewers, for constructive comments and suggestions related to this manuscript. The authors gratefully acknowledge the use of the ERAU Vega High-Performance Computing Cluster and New Zealand's NeSI Computing Cluster.

References

Afraimovich, E. L., Astafyeva, E. I., Demyanov, V. V., Edemskiy, I. K., Gavrilyuk, N. S., Ishin, A. B., et al. (2013). A review of GPS/GLONASS studies of the ionospheric response to natural and anthropogenic processes and phenomena. *Journal of Space Weather and Space Climate*, *3*, A27. https://doi.org/10.1051/swsc/2013049

Afraimovich, E. L., Perevalova, N. P., Plotnikov, A. V., & Uralov, A. M. (2001). The shock-acoustic waves generated by earthquakes. *Annales Geophysicae*, *19*(4), 395–409. https://doi.org/10.5194/angeo-19-395-2001

Ando, R., & Kaneko, Y. (2018). Dynamic rupture simulation reproduces spontaneous multifault rupture and arrest during the 2016 Mw 7.9 Kaikoura Earthquake. *Geophysical Research Letters*, *45*, 12875–12883. https://doi.org/10.1029/2018GL080550

Archuleta, R. J., Ji, C., & Adams, M. N. (2018). *Strong ground motion from earthquakes with multiple faults*. Paper presented at SMIP18 Seminar on Utilization of Strong-Motion Data Proceedings.

Astafyeva, E. (2019). Ionospheric detection of natural hazards. *Reviews of Geophysics*, *57*, 1265–1288. https://doi.org/10.1029/2019RG000668

Astafyeva, E., Heki, K., Kiryushkin, V., Afraimovich, E., & Shalimov, S. (2009). Two-mode long-distance propagation of coseismic ionosphere disturbances. *Journal of Geophysical Research*, *114*, A10307. https://doi.org/10.1029/2008JA013853

Astafyeva, E., Shalimov, S., Olshanskaya, E., & Lognonné, P. (2013). Ionospheric response to earthquakes of different magnitudes: Larger quakes perturb the ionosphere stronger and longer. *Geophysical Research Letters*, *40*, 1675–1681. https://doi.org/10.1002/grl.50398

Astafyeva, E., & Shults, K. (2019). Ionospheric GNSS imagery of seismic source: Possibilities, difficulties, and challenges. *Journal of Geophysical Research: Space Physics*, *124*, 534–543. https://doi.org/10.1029/2018JA026107

Azeem, I., Vadas, S. L., Crowley, G., & Makela, J. J. (2017). Traveling ionospheric disturbances over the united states induced by gravity waves from the 2011 Tohoku tsunami and comparison with gravity wave dissipative theory. *Journal of Geophysical Research: Space Physics*, *122*, 3430–3447. https://doi.org/10.1002/2016JA023659

Bagiya, M. S., Sunil, P. S., Sunil, A. S., & Ramesh, D. S. (2018). Coseismic contortion and coupled nocturnal ionospheric perturbations during 2016 Kaikoura, Mw 7.8 New Zealand Earthquake. *Journal of Geophysical Research: Space Physics*, *123*, 1477–1487. https://doi.org/10.1002/2017JA024584

Bai, Y., Lay, T., Cheung, K. F., & Ye, L. (2017). Two regions of seafloor deformation generated the tsunami for the 13 November 2016, Kaikoura, New Zealand earthquake. *Geophysical Research Letters*, *44*, 6597–6606. https://doi.org/10.1002/2017GL073717

Becker, J. J., Sandwell, D. T., Smith, W. H. F., Braud, J., Binder, B., Depner, J., et al. (2009). Global bathymetry and elevation data at 30 arc seconds resolution: Srtm30_plus. *Marine Geodesy*, *32*(4), 355–371.

Beyer, R. T. (1974). *Nonlinear acoustics*. Washington: The Command.

Bittner, M., Höppner, K., Pilger, C., & Schmidt, C. (2010). Mesopause temperature perturbations caused by infrasonic waves as a potential indicator for the detection of tsunamis and other geo-hazards. *Natural Hazards and Earth System Sciences*, *10*(7), 1431–1442. https://doi.org/10.5194/nhess-10-1431-2010

Blanc, E. (1985). Observations in the upper atmosphere of infrasonic waves from natural or artificial sources: A summary. *Annales Geophysicae*, *3*, 673–687.

Bolt, B. A. (1964). Seismic air waves from the great 1964 Alaskan earthquake. *Nature*, *202*(4937), 1095–1096.

Calais, E., & Minster, J. B. (1998). GPS, earthquakes, the ionosphere, and the Space Shuttle. *Physics of the Earth and Planetary Interiors*, *105*(3), 167–181. https://doi.org/10.1016/S0031-9201(97)00089-7

Carlson, H. W., Mack, R. J., & Morris, O. A. (1966). Sonic-boom pressure-field estimation techniques. *Journal of the Acoustical Society of America*, *39*(5B), S10–S18. https://doi.org/10.1121/1.1914038

Carlson, H. W., & Maglieri, D. J. (1972). Review of sonic-boom generation theory and prediction methods. *Journal of the Acoustical Society of America*, *51*(2C), 675–685. https://doi.org/10.1121/1.1912901

Catherine, J. K., Uma Maheshwari, D., Gahalaut, V. K., Roy, P. N. S., Khan, P. K., & Puviarasan, N. (2017). Ionospheric disturbances triggered by the 25 April, 2015 M7.8 Gorkha earthquake, Nepal: Constraints from GPS TEC measurements. *Journal of Asian Earth Sciences*, *133*, 80–88. https://doi.org/10.1016/j.jseaes.2016.07.014

Cesca, S., Zhang, Y., Mouslopoulou, V., Wang, R., Saul, J., Savage, M., et al. (2017). Complex rupture process of the Mw 7.8, 2016, Kaikoura earthquake, New Zealand, and its aftershock sequence. *Earth and Planetary Science Letters*, *478*, 110–120. https://doi.org/10.1016/j.epsl.2017.08.024

Chou, M. Y., Lin, C. C. H., Yue, J., Tsai, H. F., Sun, Y. Y., Liu, J. Y., & Chen, C. H. (2017). Concentric traveling ionosphere disturbances triggered by Super Typhoon Meranti (2016). *Geophysical Research Letters*, *44*, 1219–1226. https://doi.org/10.1002/2016GL072205

Chum, J., Hruska, F., Zednik, J., & Lastovicka, J. (2012). Ionospheric disturbances (infrasound waves) over the Czech Republic excited by the 2011 Tohoku earthquake. *Journal of Geophysical Research*, *117*, A08319. https://doi.org/10.1029/2012JA017767

Clark, K. J., Nissen, E. K., Howarth, J. D., Hamling, I. J., Mountjoy, J. J., Ries, W. F., et al. (2017). Highly variable coastal deformation in the 2016 Mw 7.8 Kaikōura earthquake reflects rupture complexity along a transpressional plate boundary. *Earth and Planetary Science Letters*, *474*, 334–344. https://doi.org/10.1016/j.epsl.2017.06.048

Crow, S. C. (1969). Distortion of sonic bangs by atmospheric turbulence. *Journal of Fluid Mechanics*, *37*(3), 529–563. https://doi.org/10.1017/S0022112069000711

Diederichs, A., Nissen, E. K., Lajoie, L. J., Langridge, R. M., Malireddi, S. R., Clark, K. J., et al. (2019). Unusual kinematics of the Papatea fault (2016 Kaikōura earthquake) suggest anelastic rupture. *Science Advances*, *5*(10), eaax5703. https://doi.org/10.1126/sciadv.aax5703

Drob, D. P., Emmert, J. T., Meriwether, J. W., Makela, J. J., Doornbos, E., Conde, M., et al. (2015). An update to the Horizontal Wind Model (HWM): The quiet time thermosphere. *Earth and Space Science*, *2*, 301–319. https://doi.org/10.1002/2014EA000089

Eberhart-Phillips, D., Bannister, S., & Reyners, M. (2017). Deciphering the 3-D distribution of fluid along the shallow Hikurangi subduction zone using P- and S-wave attenuation. *Geophysical Journal International*, *211*(2), 1032–1045. https://doi.org/10.1093/gji/ggx348
Eberhart-Phillips, D., Reyners, M., & Bannister, S. (2015). A 3D QP attenuation model for all of New Zealand. *Seismological Research Letters*, *86*, 1655–1663. https://doi.org/10.1785/0220150124
Galvan, D. A., Komjathy, A., Hickey, M. P., Stephens, P., Snively, J., Tony Song, Y., et al. (2012). Ionospheric signatures of Tohoku-Oki tsunami of March 11, 2011: Model comparisons near the epicenter. *Radio Science*, *47*, RS4003. https://doi.org/10.1029/2012RS005023
Georges, T. M., & Hooke, W. H. (1970). Wave-induced fluctuations in ionospheric electron content: A model indicating some observational biases. *Journal of Geophysical Research*, *75*(31), 6295–6308. https://doi.org/10.1029/JA075i031p06295
Godin, O. A. (2006). Anomalous transparency of water–air interface for low-frequency sound. *Physical Review Letters*, *97*, 164301. https://doi.org/10.1103/PhysRevLett.97.164301
Godin, O. A., Zabotin, N. A., & Zabotina, L. (2020). Atmospheric resonances and their coupling to vibrations of the ground and waves in the ocean. *Earth, Planets and Space*, *72*(1), 1–19.
Hamling, I. J., Hreinsdóttir, S., Clark, K., Elliott, J., Liang, C., Fielding, E., et al. (2017). Complex multifault rupture during the 2016 Mw 7.8 Kaikōura earthquake, New Zealand. *Science*, *356*(6334), eaam7194. https://doi.org/10.1126/science.aam7194
Heidarzadeh, M., & Satake, K. (2017). Possible dual earthquake–landslide source of the 13 November 2016 Kaikoura, New Zealand tsunami. *Pure and Applied Geophysics*, *174*(10), 3737–3749. https://doi.org/10.1007/s00024-017-1637-4
Hines, C. O. (1960). Internal atmospheric gravity waves at ionospheric heights. *Canadian Journal of Physics*, *38*(11), 1441–1481. https://doi.org/10.1139/p60-150
Holden, C., Kaneko, Y., D'Anastasio, E., Benites, R., Fry, B., & Hamling, I. J. (2017). The 2016 Kaikōura earthquake revealed by kinematic source inversion and seismic wavefield simulations: Slow rupture propagation on a geometrically complex crustal fault network. *Geophysical Research Letters*, *44*, 11320–11328. https://doi.org/10.1002/2017GL075301
Howes, W. L. (1967). Farfield spectrum of the sonic boom. *Journal of the Acoustical Society of America*, *41*(3), 716–717. https://doi.org/10.1121/1.1910402
Igel, H. (2017). *Computational seismology, a practical introduction*. Oxford, UK: Oxford University Press.
Inchin, P. A., Snively, J. B., Williamson, A., Melgar, D., Aguilar Guerrero, J., & Zettergren, M. D. (2020). Mesopause airglow disturbances driven by nonlinear infrasonic acoustic waves generated by large earthquakes. *Journal of Geophysical Research: Space Physics*, *125*, e2019JA027628. https://doi.org/10.1029/2019JA027628
Inchin, P. A., Snively, J. B., Zettergren, M. D., Komjathy, A., Verkhoglyadova, O. P., & Tulasi Ram, S. (2020). Modeling of ionospheric responses to atmospheric acoustic and gravity waves driven by the 2015 Nepal Mw 7.8 Gorkha earthquake. *Journal of Geophysical Research: Space Physics*, *125*, e2019JA027200. https://doi.org/10.1029/2019JA027200
Inoue, Y., & Yano, T. (1997). Propagation of strongly nonlinear plane n-waves. *Journal of Fluid Mechanics*, *341*, 59–76. https://doi.org/10.1017/S0022112097005405
Kakinami, Y., Kamogawa, M., Tanioka, Y., Watanabe, S., Gusman, A. R., Liu, J.-Y., et al. (2012). Tsunamigenic ionospheric hole. *Geophysical Research Letters*, *39*, L00G27. https://doi.org/10.1029/2011GL050159
Kamogawa, M., Orihara, Y., Tsurudome, C., Tomida, Y., Kanaya, T., Ikeda, D., et al. (2016). A possible space-based tsunami early warning system using observations of the tsunami ionospheric hole. *Scientific Reports*, *6*, 37989. https://doi.org/10.1038/srep37989
Kiser, E., & Ishii, M. (2017). Back-projection imaging of earthquakes. *Annual Review of Earth and Planetary Sciences*, *45*(1), 271–299. https://doi.org/10.1146/annurev-earth-063016-015801
Komatitsch, D., & Tromp, J. (2002). Spectral-element simulations of global seismic wave propagation—II. Three-dimensional models, oceans, rotation and self-gravitation. *Geophysical Journal International*, *150*(1), 303–318. https://doi.org/10.1046/j.1365-246X.2002.01716.x
Komatitsch, D., & Vilotte, J.-P. (1998). The spectral element method: An efficient tool to simulate the seismic response of 2D and 3D geological structures. *Bulletin of the Seismological Society of America*, *88*(2), 368–392. https://doi.org/10.1029/2005RS003279
Komjathy, A., Sparks, L., Wilson, B. D., & Mannucci, A. J. (2005). Automated daily processing of more than 1000 ground-based GPS receivers for studying intense ionospheric storms. *Radio Science*, *40*, RS6006. https://doi.org/10.1029/2005RS003279
Komjathy, A., Yang, Y.-M., Meng, X., Verkhoglyadova, O., Mannucci, A. J., & Langley, R. B. (2016). Review and perspectives: Understanding natural-hazards-generated ionospheric perturbations using GPS measurements and coupled modeling. *Radio Science*, *51*, 951–961. https://doi.org/10.1002/2015RS005910
Langridge, R. M., Rowland, J., Villamor, P., Mountjoy, J., Townsend, D. B., Nissen, E., et al. (2018). Coseismic rupture and preliminary slip estimates for the Papatea Fault and its role in the 2016 Mw 7.8 Kaikōura, New Zealand, earthquake. *Bulletin of the Seismological Society of America*, *108*, 1596–1622. https://doi.org/10.1785/0120170336
Lay, T., & Wallace, T. C. (1995). *Modern global seismology*. London: Academic Press.
Lee, R. F., Rolland, L. M., & Mikesell, T. D. (2018). Seismo-ionospheric observations, modeling, and backprojection of the 2016 Kaikōura earthquake. *Bulletin of the Seismological Society of America*, *108*(3B), 1794–1806. https://doi.org/10.1785/0120170299
Leonard, R. S., & Barnes, R. A., Jr. (1965). Observation of ionospheric disturbances following the Alaska earthquake. *Journal of Geophysical Research*, *70*(5), 1250–1253. https://doi.org/10.1029/JZ070i005p01250
Levin, B. W., & Nosov, M. A. (2016). General information on tsunami waves, seaquakes, and other catastrophic phenomena in the ocean. In *Physics of tsunamis* (pp. 1–34). Cham, Switzerland: Springer International Publishing. https://doi.org/10.1007/978-3-319-24037-4_1
Li, J. D., Rude, C. M., & Pankratius, V. (2018). Characterizing the complex two N-wave ionospheric signature of the 2016 Kaikoura earthquake. *Journal of Geophysical Research: Space Physics*, *123*, 10358–10367. https://doi.org/10.1029/2018JA025376
Litchfield, N. J., Villamor, P., Dissen, R. J. V., Nicol, A., Barnes, P. M., Barrell, D. J. A. (2018). Surface rupture of multiple crustal faults in the 2016 Mw 7.8 Kaikōura, New Zealand, earthquake. *Bulletin of the Seismological Society of America*. https://doi.org/10.1785/0120170300
Liu, T.-P. (1977). Large-time behavior of solutions of initial and initial-boundary value problems of a general system of hyperbolic conservation laws. *Communications in Mathematical Physics*, *55*(2), 163–177. https://doi.org/10.1007/bf01626518
Liu, Y., & Jin, S. (2019). Ionospheric Rayleigh wave disturbances following the 2018 Alaska earthquake from GPS observations. *Remote Sensing*, *11*(8), 901. https://doi.org/10.3390/rs11080901
Marchiano, R., Coulouvrat, F., & Thomas, J.-L. (2005). Nonlinear focusing of acoustic shock waves at a caustic cusp. *Journal of the Acoustical Society of America*, *117*(2), 566–577. https://doi.org/10.1121/1.1841551
Maruyama, T., Shinagawa, H., Yusupov, K., & Akchurin, A. (2017). Sensitivity of ionosonde detection of atmospheric disturbances induced by seismic Rayleigh waves at different latitudes. *Earth, Planets and Space*, *69*, 20. https://doi.org/10.1186/s40623-017-0600-z
Matsumura, M., Saito, A., Iyemori, T., Shinagawa, H., Tsugawa, T., Otsuka, Y., et al. (2011). Numerical simulations of atmospheric waves excited by the 2011 off the Pacific coast of Tohoku earthquake. *Earth, Planets and Space*, *63*(7), 885–889. https://doi.org/10.5047/eps.2011.07.015

McDonald, B. E., & Calvo, D. C. (2007). Enhanced sound transmission from water to air at low frequencies. *Journal of the Acoustical Society of America*, *122*(6), 3159–3161. https://doi.org/10.1121/1.2793709

Mendillo, M. (1988). Ionospheric holes: A review of theory and recent experiments. *Advances in Space Research*, *8*(1), 51–62. https://doi.org/10.1016/0273-1177(88)90342-0

Meng, X., Vergados, P., Komjathy, A., & Verkhoglyadova, O. (2019). Upper atmospheric responses to surface disturbances: An observational perspective. *Radio Science*, *54*, 1076–1098. https://doi.org/10.1029/2019RS006858

Meng, X., Verkhoglyadova, O. P., Komjathy, A., Savastano, G., & Mannucci, A. J. (2018). Physics-based modeling of earthquake-induced ionospheric disturbances. *Journal of Geophysical Research: Space Physics*, *123*, 8021–8038. https://doi.org/10.1029/2018JA025253

Mountjoy, J. J., Howarth, J. D., Orpin, A. R., Barnes, P. M., Bowden, D. A., Rowden, A. A., et al. (2018). Earthquakes drive large-scale submarine canyon development and sediment supply to deep-ocean basins. *Science Advances*, *4*(3), eaar3748. https://doi.org/10.1126/sciadv.aar3748

Nishioka, M., Tsugawa, T., Kubota, M., & Ishii, M. (2013). Concentric waves and short-period oscillations observed in the ionosphere after the 2013 Moore EF5 tornado. *Geophysical Research Letters*, *40*, 5581–5586. https://doi.org/10.1002/2013GL057963

Occhipinti, G., Aden-Antoniow, F., Bablet, A., Molinie, J.-P., & Farges, T. (2018). Surface waves magnitude estimation from ionospheric signature of Rayleigh waves measured by doppler sounder and OTH radar. *Scientific Reports*, *8*(1), 1–7. https://doi.org/10.1038/s41598-018-19305-1

Occhipinti, G., Rolland, L., Lognonné, P., & Watada, S. (2013). From Sumatra 2004 to Tohoku-Oki 2011: The systematic GPS detection of the ionospheric signature induced by tsunamigenic earthquakes. *Journal of Geophysical Research: Space Physics*, *118*, 3626–3636. https://doi.org/10.1002/jgra.50322

Parkinson, B., Spilker, J., Axelrad, P., & Enge, P. (1995). *Global Positioning System: Theory and applications* (Vol. I).

Picone, J. M., Hedin, A. E., Drob, D. P., & Aikin, A. C. (2002). NRLMSISE-00 empirical model of the atmosphere: Statistical comparisons and scientific issues. *Journal of Geophysical Research*, *107*(A12), 1468. https://doi.org/10.1029/2002JA009430

Pierce, A. D., & Maglieri, D. J. (1972). Effects of atmospheric irregularities on sonic-boom propagation. *Journal of the Acoustical Society of America*, *51*(2C), 702–721. https://doi.org/10.1121/1.1912904

Pilger, C., Schmidt, C., Streicher, F., Wüst, S., & Bittner, M. (2013). Airglow observations of orographic, volcanic and meteorological infrasound signatures. *Journal of Atmospheric and Solar-Terrestrial Physics*, *104*, 55–66. https://doi.org/10.1016/j.jastp.2013.08.008

Press, F., & Harkrider, D. (1962). Propagation of acoustic-gravity waves in the atmosphere. *Journal of Geophysical Research*, *67*(10), 3889–3908. https://doi.org/10.1029/JZ067i010p03889

Reddy, C. D., Shrivastava, M. N., Seemala, G. k., González, G., & Baez, J. C. (2017). Ionospheric plasma response to Mw 8.3 Chile Illapel earthquake on September 16, 2015. In C. Braitenberg & A. B. Rabinovich (Eds.), *The Chile-2015 (Illapel) earthquake and tsunami* (pp. 145–155). Cham, Switzerland: Springer International Publishing. https://doi.org/10.1007/978-3-319-57822-4_12

Ren, X., Zhang, X., Xie, W., Zhang, K., Yuan, Y., & Li, X. (2016). Global ionospheric modelling using multi-GNSS: Beidou, Galileo, GLONASS and GPS. *Scientific Reports*, *6*, 33499. https://doi.org/10.1038/srep33499

Rolland, L. M., Lognonné, P., & Munekane, H. (2011). Detection and modeling of Rayleigh wave induced patterns in the ionosphere. *Journal of Geophysical Research*, *116*, A05320. https://doi.org/10.1029/2010JA016060

Sabatini, R., Marsden, O., Bailly, C., & Gainville, O. (2019). Three-dimensional direct numerical simulation of infrasound propagation in the Earth's atmosphere. *Journal of Fluid Mechanics*, *859*, 754–789. https://doi.org/10.1017/jfm.2018.816

Sabatini, R., Snively, J. B., Bailly, C., Hickey, M. P., & Garrison, J. L. (2019). Numerical modeling of the propagation of infrasonic acoustic waves through the turbulent field generated by the breaking of mountain gravity waves. *Geophysical Research Letters*, *46*, 5526–5534. https://doi.org/10.1029/2019GL082456

Saito, A., Tsugawa, T., Otsuka, Y., Nishioka, M., Iyemori, T., Matsumura, M., et al. (2011). Acoustic resonance and plasma depletion detected by GPS total electron content observation after the 2011 off the Pacific coast of Tohoku Earthquake. *Earth, Planets and Space*, *63*(7), 863–867. https://doi.org/10.5047/eps.2011.06.034

Saito, T. (2019). Tsunami generation. In *Tsunami generation and propagation* (pp. 149–203). Tokyo, Japan: Springer. https://doi.org/10.1007/978-4-431-56850-6_5

Satake, K. (1987). Inversion of tsunami waveforms for the estimation of a fault heterogeneity: Method and numerical experiments. *Journal of Physics of the Earth*, *35*(3), 241–254. https://doi.org/10.4294/jpe1952.35.241

Savastano, G. (2018). *New applications and challenges of GNSS variometric approach* (Doctoral dissertation). The University of Rome "La Sapienza". Retrieved from http://hdl.handle.net/11573/1077041

Savastano, G., Komjathy, A., Shume, E., Vergados, P., Ravanelli, M., Verkhoglyadova, O., et al. (2019). Advantages of geostationary satellites for ionospheric anomaly studies: Ionospheric plasma depletion following a rocket launch. *Remote Sensing*, *11*(14), 1734. https://doi.org/10.3390/rs11141734

Savastano, G., Komjathy, A., Verkhoglyadova, O., Mazzoni, A., Crespi, M., Wei, Y., & Mannucci, A. J. (2017). Real-time detection of tsunami ionospheric disturbances with a stand-alone GNSS receiver: A preliminary feasibility demonstration. *Scientific Reports*, *7*, 46607. https://doi.org/10.1038/srep46607

Shults, K., Astafyeva, E., & Adourian, S. (2016). Ionospheric detection and localization of volcano eruptions on the example of the April 2015 Calbuco events. *Journal of Geophysical Research: Space Physics*, *121*, 10303–10315. https://doi.org/10.1002/2016JA023382

Smoller, J. (2012). *Shock waves and reaction—Diffusion equations* (Vol. 258). New York, Springer Science & Business Media.

Snively, J. B. (2013). Mesospheric hydroxyl airglow signatures of acoustic and gravity waves generated by transient tropospheric forcing. *Geophysical Research Letters*, *40*, 4533–4537. https://doi.org/10.1002/grl.50886

Sunil, A. S., Bagiya, M. S., Catherine, J., Rolland, L., Sharma, N., Sunil, P. S., & Ramesh, D. S. (2017). Dependence of near field co-seismic ionospheric perturbations on surface deformations: A case study based on the April, 25 2015 Gorkha Nepal earthquake. *Advances in Space Research*, *59*(5), 1200–1208. https://doi.org/10.1016/j.asr.2016.11.041

Tan, F., Ge, Z., Kao, H., & Nissen, E. (2019). Validation of the 3-D phase-weighted relative back projection technique and its application to the 2016 Mw 7.8 Kaikōura earthquake. *Geophysical Journal International*, *217*(1), 375–388. https://doi.org/10.1093/gji/ggz032

Teunissen, P., & Montenbruck, O. (2017). *Springer handbook of global navigation satellite systems*. Cham, Switzerland: Springer.

Thomas, D., Bagiya, M. S., Sunil, P. S., Rolland, L., Sunil, A. S., Mikesell, T. D., et al. (2018). Revelation of early detection of co-seismic ionospheric perturbations in GPS-TEC from realistic modeling approach: Case study. *Scientific Reports*, *8*, 2045–2322. https://doi.org/10.1038/s41598-018-30476-9

Ulrich, T., Gabriel, A.-A., Ampuero, J.-P., & Xu, W. (2019). Dynamic viability of the 2016 Mw 7.8 Kaikōura earthquake cascade on weak crustal faults. *Nature Communications*, *10*(1), 1213. https://doi.org/10.1038/s41467-019-09125-w

Van Dissen, R., & Yeats, R. S. (1991). Hope fault, Jordan thrust, and uplift of the Seaward Kaikoura Range, New Zealand. *Geology*, *19*(4), 393–396. https://doi.org/10.1130/0091-7613(1991)019<0393:HFJTAU>2.3.CO;2

Wallace, L. M., Barnes, P., Beavan, J., Van Dissen, R., Litchfield, N., Mountjoy, J., et al. (2012). The kinematics of a transition from subduction to strike-slip: An example from the central New Zealand plate boundary. *Journal of Geophysical Research*, *117*, B02405. https://doi.org/10.1029/2011JB008640

Wang, T., Wei, S., Shi, X., Qiu, Q., Li, L., Peng, D., et al. (2018). The 2016 Kaikōura earthquake: Simultaneous rupture of the subduction interface and overlying faults. *Earth and Planetary Science Letters*, *482*, 44–51. https://doi.org/10.1016/j.epsl.2017.10.056

Whitham, G. (1974). *Linear and nonlinear waves*. New York: Wiley-Interscience.

Xu, W., Feng, G., Meng, L., Zhang, A., Ampuero, J. P., Bürgmann, R., & Fang, L. (2018). Transpressional rupture cascade of the 2016 Mw 7.8 Kaikoura earthquake, New Zealand. *Journal of Geophysical Research: Solid Earth*, *123*, 2396–2409. https://doi.org/10.1002/2017JB015168

Zettergren, M. D., & Snively, J. B. (2015). Ionospheric response to infrasonic-acoustic waves generated by natural hazard events. *Journal of Geophysical Research: Space Physics*, *120*, 8002–8024. https://doi.org/10.1002/2015JA021116

Zettergren, M. D., Snively, J. B., Komjathy, A., & Verkhoglyadova, O. P. (2017). Nonlinear ionospheric responses to large-amplitude infrasonic-acoustic waves generated by undersea earthquakes. *Journal of Geophysical Research: Space Physics*, *122*, 2272–2291. https://doi.org/10.1002/2016JA023159

Zettergren, M., & Semeter, J. (2012). Ionospheric plasma transport and loss in auroral downward current regions. *Journal of Geophysical Research*, *117*, A06306. https://doi.org/10.1029/2012JA017637

Zhang, H., Koper, K. D., Pankow, K., & Ge, Z. (2017). Imaging the 2016 Mw 7.8 Kaikoura, New Zealand, earthquake with teleseismic P waves: A cascading rupture across multiple faults. *Geophysical Research Letters*, *44*, 4790–4798. https://doi.org/10.1002/2017GL073461

Detail of forward seismic wave simulation method

We simulate seismic wave propagation resulting from the Kaikoura earthquake using open-source seismic wave propagation software SPECFEM3D (Komatitsch & Vilotte, 1998; Komatitsch & Tromp, 2002). The computational domain is 1200 km by 600 km at the Earth surface, extends to 400 km depth and includes local topography and bathymetry. The mesh contains 4.7 million spectral elements with the average spacing between Gauss-Lobatto-Legendre node points at the Earth surface is 250 m. The minimum values of Vp, Vs and density are 1.7 km/s, 0.98 km/s and 1.7 g/cm^3, respectively. The seismic waves are numerically resolved down to a period of 2.5 s. Topography and bathymetry are interpolated from SRTM-30P (Becker *et al.* 2009). All the seismic stations are placed on the Earth's surface (i.e., on the topography). To compute time-dependent surface displacement used as an input for the IAW propagation code, a grid of receivers with a spatial resolution of 1.0 km is additionally placed on the Earth's surface. A water layer is not included in this mesh. A mesh depth of 400 km is chosen to mitigate the effect of artificial wave reflections from the bottom boundary.

We compare simulated surface velocities to 3 component velocity waveform data from a total of 17 regional stations comprised of 14 strong motion stations and 3 high-rate GPS sites from the New Zealand GeoNet network (e.g., Figure 2). The acceleration waveforms are integrated into velocity and filtered using a Butterworth bandpass filter from 0.01 to 0.3333 Hz (a period band of 3 to 100 s). The GPS velocity waveforms are derived from the time derivative of displacement waveforms, which are then bandpass-filtered at the same frequency range.

Becker, J., *et al.*, 2009. Global bathymetry and elevation data at 30 arc seconds resolution: SRTM30 PLUS, *Mar. Geod.,* **32**(4), 355–371.

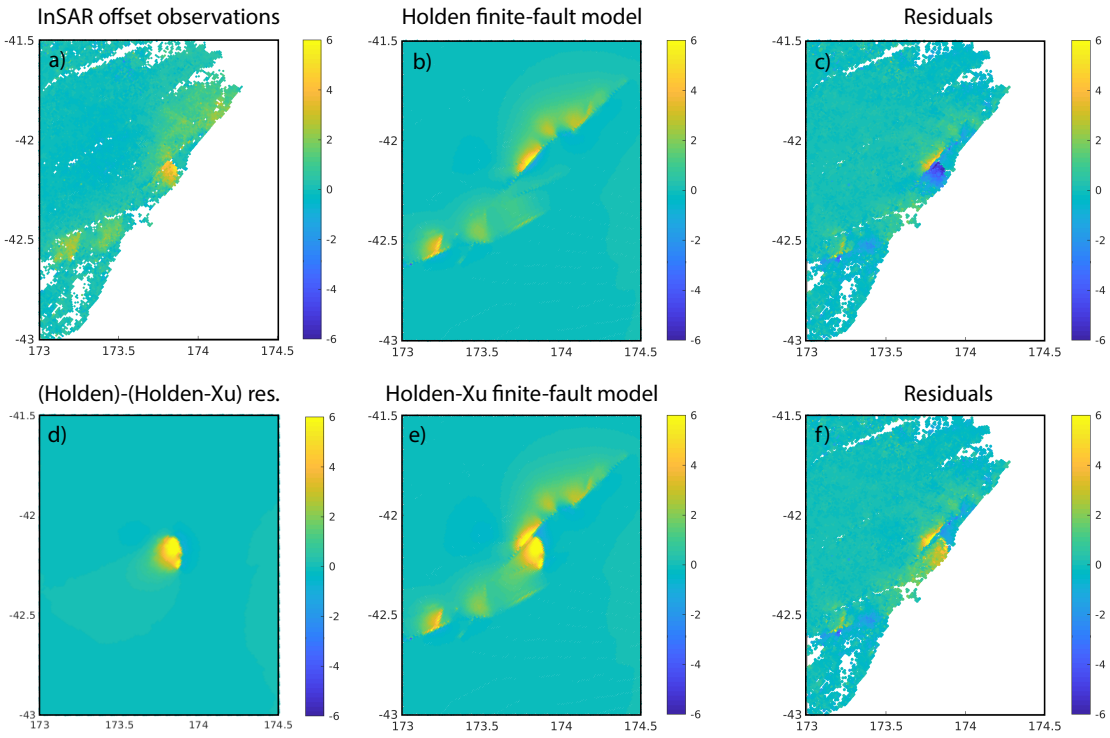

Comparison between (a) observed and (b, d) simulated vertical displacement field for the original Holden model and Holden-Xu model and (c, d) their residuals. The overall residual in the region around the Papatea fault (indicated by the black rectangle) is smaller in the Holden-Xu model (root-mean-square misfit of 2.39) than the original Holden model (root-mean-square misfit of 2.67). Note that, in both of these models, the deformation is slightly overestimated in general, because the final slip distributions were previously obtained assuming a homogeneous elastic halfspace (Clark et al., 2017; Xu et al., 2018) as opposed to a 3D velocity model accounting for lower rigidity rocks at shallow depths assumed in our simulations.

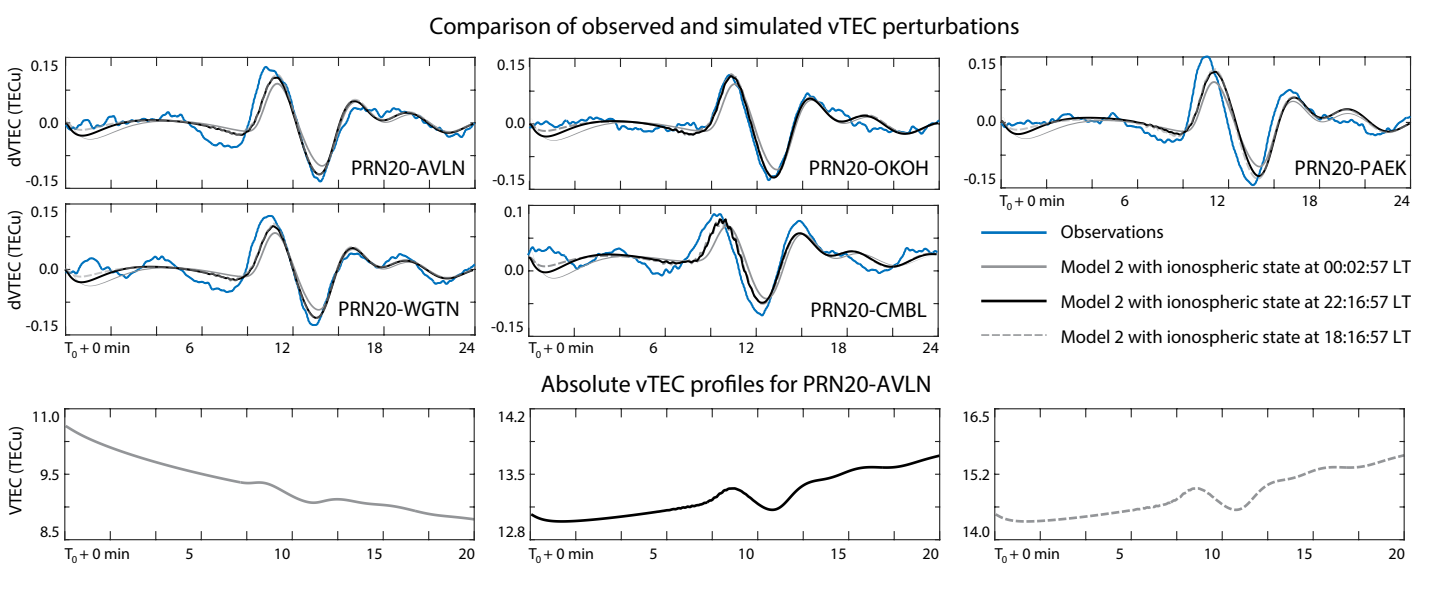
Comparison of observed and simulated vTEC perturbations
dVTEC (TECu)
0.15
0.0
-0.15
PRN20-AVLN
PRN20-OKOH
PRN20-PAEK
PRN20-WGTN
PRN20-CMBL
0.1
T0 + 0 min
6
12
18
24
Observations
Model 2 with ionospheric state at 00:02:57 LT
Model 2 with ionospheric state at 22:16:57 LT
Model 2 with ionospheric state at 18:16:57 LT
Absolute vTEC profiles for PRN20-AVLN
VTEC (TECu)
11.0
9.5
8.5
14.2
13.5
12.8
16.5
15.2
14.0
5
10
15
20